State-dependent processing of Dentate Gyrus granule cell activity *in-vivo*

Dissertation

zur

Erlangung des Doktorgrades (Dr. rer. nat.)

der

Mathematisch-Naturwissenschaftlichen Fakultät

der

Rheinischen Friedrich-Wilhelms-Universität Bonn

vorgelegt von

Martin Pofahl

aus

Bergisch Gladbach

Bonn, August 18, 2020

Angefertigt mit Genehmigung der Mathematisch-Naturwissenschaftlichen Fakultät der Rheinischen Friedrich-Wilhelms-Universität

1. Gutachter:	Prof. Dr. Heinz Beck
2. Gutachter:	Prof. Dr. Walter Witke

Tag der Promotion:	December 2, 2020
Erscheinungsjahr:	2020

Abstract

The ability to form dissimilar neural activity patterns from similar sensory driven inputs is a phenomenon found in all vertebrates, called pattern separation. In mammals, pattern separation is closely related to a subregion of the hippocampus, namely the dentate gyrus. The dentate gyrus is an important relay conveying sensory information from the entorhinal cortex to the hippocampus proper and is characterized by a large number of rarely active granule cells that generate a very sparse neural code. While the coding features of granule cells during locomotion have been the subject of several studies, the dentate gyrus also shows activity patterns during immobility and sleep. However, the cellular composition of these patterns and their role in behavior remain elusive.

In this thesis we used dual color two photon-Ca^{2+}-imaging in mice to visualize the activity of perforant path input fibers as well as the activity of individual dentate granule cells. We developed a novel approach of head fixation and cranial window design in order to gain visual access to the dentate gyrus. This enabled the recording of neural activity in head fixed mice running on a linear track. Using this approach we found sparse synchronized activity patterns that we termed network events. These network events emerged exclusively during immobility and were associated with distinct activations of the perforant path input. Interestingly, network events incorporate place and speed cells and their features are sensitive to changes in the environment. To compare the population coding during locomotion ant network activity we utilized principal component analysis in different behavioral states. Using this approach we could show that locomotion related population patterns are recapitulated during network events in immobile animals.

Contents

Chapter 1

Introduction

The human brain contains more than 10^{11} neurons, nerve cells that encode our thinking, memory and behavior [1]. This large number is necessary to achieve a certain level of complex connectivity needed for brain function. The mouse brain with its 10^6 neurons cannot achieve similar functionality as the human brain [2]. Nevertheless, mice achieve complex decision making based on external and internal information and memory based models. They do this with a brain that shares many anatomical features with the human brain. Thus, the mouse brain offers a suitable model to study fundamental archetypes of memory and behavior.

Neurons are arranged in networks that receive information, perform computations and generate functional outputs. Functional outputs are forwarded to efferent layers of neuronal networks and may in the end trigger a response. Responses can be manifold and whether that response is, for example, the initiation of motor behavior, the dilation of the pupil or a decision about which way to go, is depending on the involved cascade of neuronal networks and what input initially triggered it. Possible inputs can vary from external stimuli, like direct sensory inputs, but also changes in internal states, like hunger, fatigue and, importantly, memories. Memories are an essential part determining behavior, especially for the process of decision making. A reliable formation of memories crucially depends on the plasticity of neuronal networks to adapt to new stimuli and learn appropriate responses.

The brain structure that serves a major role for learning and memory is the hippocampus [3–5]. The hippocampus consists of several neuronal layers, which are formed by the pyramidal cell layers of cornu armonis (CA) and the dentate gyrus (DG)[6]. The DG forms the initial stage of hippocampal information processing. It serves the major role of generating distinct representations of input patterns even when these patterns are similar or overlapping. This feature of input orthogonalization is called pattern separation [7–13]. However, how separated patterns are represented on a cellular level and how they contribute to the formation of memories is still unclear.

1.1 Neuronal computations

Neurons in different parts of the brain serve different purposes. There are two main features all neurons have in common. Firstly, they form connections to each other, called synapses, through which activity is passed on to efferent cells. Secondly, neurons integrate received inputs over time and elicit a stereotypical electrochemical event, termed action potential (AP), when an internal threshold is reached,. APs are therefore all-or-none events where information is coded by rate and pattern of APs. This will be further discussed in section 1.1.1. Ensembles of interconnected neurons form neuronal networks. These networks consist of different types of neurons where the main difference between neurons is whether their impact on an efferent cell is excitatory or inhibitory. Excitatory neurons are termed principal cells and they form connections between brain regions. Through these long-range connections they receive and forward activity from/to afferent parts of the brain or peripheral parts of the nervous system. Inhibitory neurons, so called interneurons, are smaller in number compared to principal cells, are extremely diverse, and serve many different functions. They mainly form short range connections that locally inhibit principal cells as well as other interneurons. This leads to an interplay of principal cells and interneurons that forms defined circuit motifs [14, 15], which will be described in detail in section 1.1.2. On a larger scale, excitation and inhibition are two opposite driving forces that can form oscillating systems and lead to network oscillations [16]. The different types of network oscillations and in which states they can be found will be discussed in section 1.1.3. The combined AP rates synchrony of all cells within a neuronal network represents the encoded information and sets up the neuronal code. The composition of these features makes neuronal networks suitable for different kinds of computation [7] and will be discussed in section 1.1.4.

1.1.1 Excitation and inhibition

Every neuron in its resting state is at an electrochemical equilibrium. This equilibrium is maintained through active and passive mechanisms in the cell membrane that conduct or pump ions. The transmembrane ion current at the cell's resting state is described by the conductance g_{rest}. This conductance builds up an ion gradient between the cytosol inside the cell and the surrounding cerebrospinal fluid (CSF) that creates a potential difference through the membrane, the resting membrane potential V_{rest} usually around $-60\,\text{mV}$ to $-80\,\text{mV}$. This leads to a leak current I_{leak} whenever the membrane voltage is forced off the equilibrium. This in turn sets up a driving force towards the resting membrane potential that can be described using Ohm's law

$$I_{\text{leak}} = g_{\text{rest}}(V(t) - V_{\text{rest}}), \tag{1.1}$$

where $V(t)$ is the membrane potential at time t. The membrane potential is forced to move away from its equilibrium through the synaptic inputs it receives at its dendrites as well as the soma. Synaptic inputs can be either excitatory or inhibitory depending on the neuro-

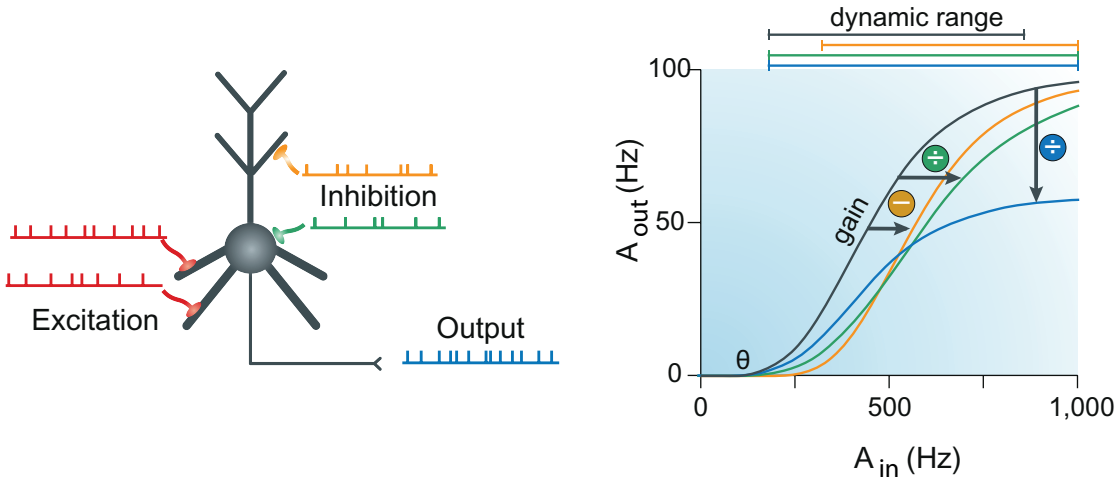

Figure 1.1 – Input-output computation of a neuron. Left side: A cell is driven by synaptic excitatory inputs (red). It receives inhibitory signals at its dendrites (yellow) as well as the soma (green). Integrated input triggers output activity (blue). Right side: Idealized input-output curve (gray line) of a signal neuron with output frequency plotted against combined input activities of afferent cells. The lower end of the dynamic range is defined by the AP threshold θ and the slope of the curve defines the gain of the response. The upper end of the curve is given by the maximum frequency of the cell. Feed forward inhibition at cell dendrites has an subtractive effect and shifts the input-output curve to higher input frequencies (yellow line). Feed forward inhibition at the soma has an normalizing effect on the input that shifts the saturation point to higher frequencies and thereby enlarges the dynamic range (green line). Feed-back inhibition has an normalizing effect on the output activity that decreases the maximal output frequency and also enlarges the dynamic range (blue line). Modified from [17].

transmitter that is released by the presynaptic cell. Excitatory neurotransmitters, mainly glutamate, trigger ionic conductances, here summarized as an excitatory conductance g_{ex}, in the cell membrane that drive the membrane potential towards the the excitatory reversal potential V_{ex}. The activation of excitatory conductance leads to the excitatory current

$$I_{ex} = g_{ex}(V(t) - V_{ex}) \tag{1.2}$$

The linked net depolarization of the cell is termed excitatory post synaptic potential (EPSP) that drives the cell towards its AP threshold. Analogously, synaptic inputs that lower the value of the membrane potential (that re- or even hyperpolarize the cell) are called inhibitory post synaptic potentials (IPSPs). The inhibitory reversal potential V_{inh} usually lies below the resting membrane potential and the corresponding inhibitory current is given as

$$I_{inh} = g_{inh}(V(t) - V_{inh}), \tag{1.3}$$

where g_{inh} is the inhibitory conductance that is triggered by inhibitory neurotransmitters, mainly γ-aminobutric acid (GABA). If inhibition occurs at the dendritic tree the in inhibitory current is subtracted from the total membrane current I_m [18]. Thus, I_m is the sum of excitatory, inhibitory, leak current and the capacitive current component

$$I_{\mathrm{m}}(t) = C_{\mathrm{m}}\frac{dV}{dt} + g_{\mathrm{rest}}(V(t) - V_{\mathrm{rest}}) + g_{\mathrm{ex}}(t)(V(t) - V_{\mathrm{ex}}) + g_{\mathrm{inh}}(t)(V(t) - V_{\mathrm{inh}}), \tag{1.4}$$

where C_{m} is capacitance of the cell membrane [19–21].

Both inhibitory and excitatory inputs are integrated from all synapses over time. As a first approximation, inputs are integrated in a linear manner and the induced currents for N afferent excitatory neurons and M interneurons can be written as

$$I_{\mathrm{ex}} = \sum_{n}^{N} w_n A_n, \qquad I_{\mathrm{inh}} = \sum_{m}^{M} w_m A_m, \tag{1.5}$$

where A_i are the activity rates of input neurons and w_i are efficacy coefficients whose value specifies the strength of the synaptic connections [22]. When the cell reaches threshold θ the output activity A_{out} can be described using the transfer-function

$$A_{\mathrm{out}} = \Gamma(I_{\mathrm{m}} - \theta)\Theta(I_{\mathrm{m}} - \theta), \tag{1.6}$$

where $\Theta(x)$ is the non-linear step function that equals 1 for $x > 0$ and 0 for $x < 0$. The AP frequency above threshold is defined by the gain Γ. The gain is a function of the input current and defines the slope of the input-output curve as schematically shown in fig. 1.1. This slope denotes the cell response sensitivity within its dynamic range. This simplified view of neuronal integration illustrates the transfer of excitatory and inhibitory inputs into activity. However, different types of ionotropic channels, voltage gated ion channels, passive dendritic cable properties and active amplification mechanisms can add non-linear components to the integration [17]. Also, currents during APs are not covered by this description. Further, recursive connections introduce discrete dependencies of the individual activity rates between neurons that can shape the input-output curve. Some of these connections between excitatory neurons and interneurons set up stereotypical circuit motifs.

1.1.2 Circuit motifs

Besides the integrative properties of neurons, another defining feature for the input-output relation of cells is the interplay between excitatory cells and inhibitory interneurons. This interplay not only affects individual neurons but is crucial for the input-output relation of the whole neuronal network [15, 24]. Although GABAergic interneurons represent only 10 to 20 % of neurons across brain areas, interneuron populations are highly heterogenic and differ in morphology, connectivity, gene expression, and electrophysiological properties [25, 26]. Interneurons have different driving forces within the network and innervate not only principal cells but also other interneurons. This forms defined circuit motifs that serve different purposes (fig. 1.2).

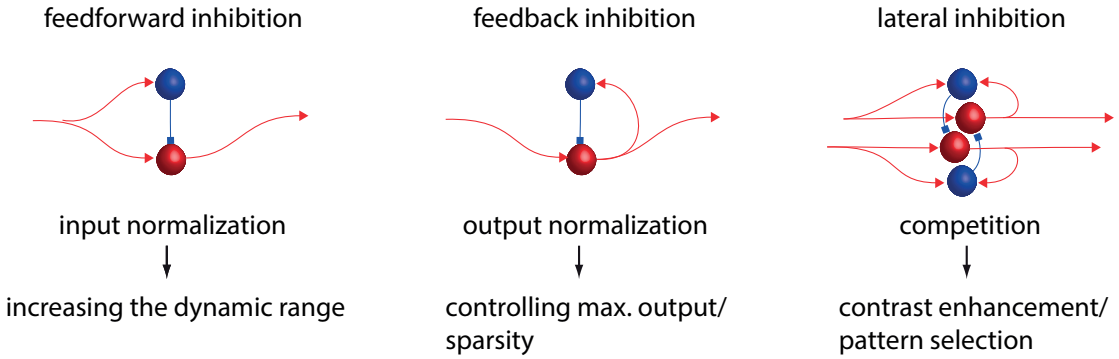

Figure 1.2 – Circuit motifs of excitatory and inhibitory neurons. Left: Feed forward inhibition is mediated by interneurons that are driven by the same input as the excitatory neurons they target. Middle: Feedback inhibition works through interneurons that are activated by the same principal cells as they project on. Right: Lateral inhibition are feedback as well as feed forward motifs the project on specifically on neighboring neurons. Modified from [23].

Feed forward inhibition

Interneurons in a feed forward circuitry share the same input as their target cells. This circuit motif can have two different functions: When feed forward inhibition happens at the dendrite it directly balances the driving input by subtraction (see formula 1.4 and fig. 1.1 yellow line) [18]. When inhibitory synapses innervate the soma, it has a more global impact on the targeted neuron. Mathematically this can be described by a division of the excitatory by the inhibitory current (fig. 1.1 green line). This process can be understood as a normalization of afferent input strength [27–29]. The inhibitory feed forward current I_{ff} is dependent on the activity of the N efferent excitatory neurons and connected through

$$I_{\text{ff}} = \sum_{n}^{N} \alpha_n A_n, \tag{1.7}$$

where α_i are effective weights, assuming that the interneurons are mostly driven above threshold so that the transition between the efferent activity and the input current can be assumed linear. Using the formalism as described by [30] the normalized excitatory input current can be written as

$$I_{\text{norm}} = \vartheta \frac{I_{\text{ex}}^k}{\sigma + I_{\text{ff}}^p}, \tag{1.8}$$

where ϑ can be interpreted as the gain and σ as the basic attenuation in the feed forward process. k and p are free parameters that balance the strength of the excitatory and the inhibitory current, respectively. Combining formula 1.8, 1.7 and 1.5 the normalized input current can be written as

$$I_{\text{norm}} = \vartheta \frac{\left(\sum_n^N w_n A_n\right)^k}{\sigma + \left(\sum_n^N \alpha_n A_n\right)^p} \tag{1.9}$$

This mechanism avoids saturation and increases the dynamic range of the individual cell [31] as well as that of the whole neural network [32].

Feed-back inhibition

Feed-back inhibition is defined by interneurons which are activated by the same excitatory pool they target. This inhibitory back projection is correlated to activity of the target ensemble leading to a global adjustment of its activity level and a normalization of the output firing rate (fig. 1.1 blue line)[30]. Analogously to formula 1.7, the feed-back current I_{fb} for a pool of K neurons in the target pool can be defined as

$$I_{\text{fb}} = \sum_k^K \beta_k A_{\text{out}}, \tag{1.10}$$

again with effective weights β_i. Feed-back projections mainly target the soma, hence they have a normalizing effect like formula 1.9. Due to the time course of synaptic transmission, the feed-back inhibition affects the integration with a delay of $\sim 10\,\text{ms}$ ($\sim 5\,\text{ms}$ for feed forward inhibition). The effectiveness of somatic inhibition at controlling AP initiation together with the delayed impact defines time windows that can be crucial for AP generation and dendritic plasticity [28, 33, 34]. Since only a certain number k of neurons is able to fire in this time window before the network is inhibited, this process is called k-winner takes it all [35]. Generally, the function of feed-back inhibition differs dramatically if it happens recursive onto the driving neuron, laterally targeted on neighboring neurons, or globally on the whole population.

Lateral inhibition

Lateral inhibition means that the excitatory drive onto a neuron or its own activity recruits interneurons which target the neighboring neurons of the same population. Thus, this process can happen in a feed forward as well as in a feed-back configuration (See fig. 1.2). Lateral inhibition has been termed the fundamental mechanism for the selection of neuronal groups [36]. Inputs that target specified (learned) sub-ensembles can laterally inhibit the rest of the population. This sharpens specified subpopulations and increases the contrast of the neuronal response [31]. Lateral feed-back inhibition triggers the competition between neurons, since the first neurons to fire will inhibit the other members of the population. This process is another k-winner takes it all mechanism. In this case the winner's activity continues which is especially suited to strengthen activity patterns [37, 38].

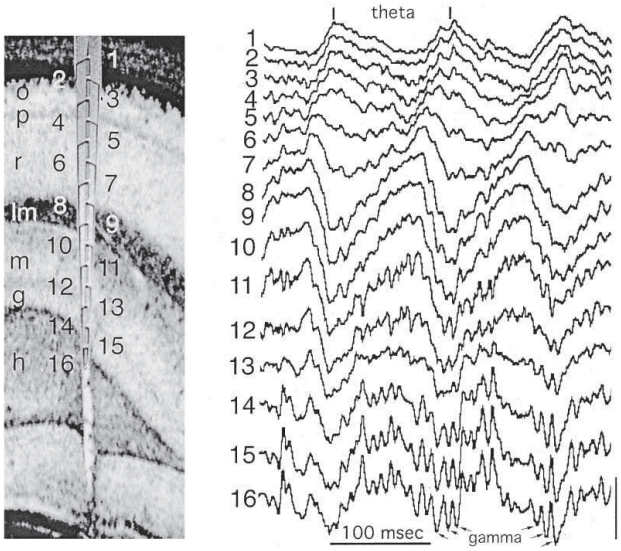

Figure 1.3 – θ-oscillations in the rat hippocampus. Left: Recording site with a 16-site silicon probe in the CA1-dentate gyrus axis. Numbers indicate recording sites (100 μm spacing). Right: θ-waves recorded during exploration. γ-waves superimposed on θ-oscillation are marked by arrows. Vertical bar: 1 mV. From [46].

Circuit motifs exist not only between excitatory cells and interneurons. Feed-back mechanisms can also be excitatory. This can be mediated by certain excitatory interneurons [39, 40] and by direct recurrent excitation [41, 42]. The inhibition of inhibition (so called disinhibition) is another common motif and can be an important learning signal for the network [43, 44]. Disinhibition can also be triggered by external neuromodulatory signals and, thus, mediate a complete change of the circuit dynamics [33]. Further, the inhibition mediated between interneurons is important to create synchronicity in the network [45].

1.1.3 Network oscillations

Inhibition controls the input-output function for individual neurons. In addition, the nature of inhibitory circuits also generates different types of oscillatory behavior. Feed-back circuits set up non-linear iterative loops. Non-linearity is caused by discrete AP threshold of each neuron and iterations are due to the delay of synaptic transmission. Synchronized excitatory input acts as a driving force on the network whereas the feedback triggers a restoring force that pushes the network back to equilibrium. Thus, the neuronal network starts oscillating.

Inhibition mediated between local interneurons can lead to an oscillation at 40 to 100 Hz, the so called γ-oscillations [47, 48]. Here, interneurons share the same excitatory drive and the lateral inhibition onto each other is thought to create the rhythmic activity [45, 49]. This leads to a synchronization of principal cells as well as interneurons [46, 50].

An oscillating interneuron network can also project oscillatory activity onto other brain regions and thereby acting as pacemaker [51, 52]. An important example of that are θ-oscillations at 4 to 10 Hz [53]. Besides the drive from the external pacemaker, θ-oscillations require a long distance feedback onto the pacemaker as well as local oscillatory loops [50, 54]. Principal cells in the targeted network as well as interneurons synchronize to special phases of the θ-frequency, which also leads to a synchronization between θ- and γ-oscillation [33, 46]. This synchronization leads to a modulation of the output signal and therefore the oscillations propagate the afferent networks [46].

The presence of θ as well as γ-oscillations is thought to represent the online state of a neuronal network and an example of their cooccurrence is shown in fig. 1.3 [55]. Therefore it is not surprising that the occurrence of these oscillations has important behavioral correlates that are linked to the respective brain region [56–58]. The rhythmicity between on and off states is hypothesized to define the time window for neural integration [59]. This paces the mechanism for individual cells and cell ensembles to be activated and when plasticity mechanisms can happen. Therefore oscillations play an important role in learning and memory [35, 60]. These implications for neural coding will be further discussed in chapter 1.3.2.

A slower form of oscillation around $1-4\,\mathrm{Hz}$ are δ-oscillations. They most prominently occur during slow wave sleep [61], but activity at this frequency range also occurs in awake but immobile animals and is referred to as large-amplitude irregular activity [56, 62]. These oscillations are coupled to respiratory behavior and have been hypothesized to act as a global synchronization mechanism across the brain [63, 64].

1.1.4 Neural code

There are several ways how neurons and neural networks can encode, store and recall information. Experimental evidence for mechanisms of neural coding is mainly based on correlation experiments. In its simplest form, the activity A (see formula 1.6) of a neuron is correlated to an external stimulus that drives the input. This concept has been shown for the encoding of direct sensory input and is called "rate coding" [65]. The activity rate in a given time interval is correlated to the stimulus intensity [1] and for a network of rate coding neurons this would lead to a statistical encoding of information with a more global input-output-curve. However, rate coding cells are found in may networks, but these networks do not show an overall probabilistic encoding. Rather individual cells code specific features of the stimulus. For example, while the neural network generally encodes visual information, individual cells can be selectively rate coding for the orientation of the visual stimulus [66]. The same is true for cells that encode specific regions, so called "place cells" [67]. In humans, the concept of "Grandma-cells" describes cells that code for the concept of individual persons [68]. The existence of this feature cells illustrates the general concept of "sparse encoding" [69]. In sparse coding, a neural network is assumed to achieve a general representation of its input using a minimum number of active neurons. This follows another basic assumption, namely that the brain generally tries to minimize the amount of energy consumed [70].

Stochastic rate coding and feature cells are two extreme concepts of encoding. Single cell coding is obviously the most energy efficient case. Still, feature encoding neurons respond stochastically and are therefore not reliable. This would lead to noisy representations of input stimuli [71]. Further, information is forwarded through cascades of neural networks. Every network has a different anatomy in terms of neuron number and composition and only the first stages receive raw input from external stimuli. All efferent networks receive the precomputed input. Thus, it is unlikely that the same stimulus shows a one-to-one representation in every network where it is computed. Also, in a feature cell coding network the number or represented features is limited by the number of cells. In terms of network capacity this would be highly inefficient [72].

The case that only one single neuron encodes a feature is statistically and anatomically very unlikely. Anatomically, excitatory synaptic connections between cells forward activity and create co-active sub-ensembles [73]. Statistically, the number of cells in experiments is always drastically undersampled. Therefore, the probability of finding a feature cell would be very low if there was indeed exactly one. The fact that they can still be found as well as theoretical assumptions have motivated the hypothesis of a population code [71]. In population code different concepts are mapped by co-active sub-ensembles in the network. The number of possible different combinations of sub-ensembles defines the maximum number of different pieces of information that can be mapped [74]. This number of combinations C in a network containing N principal neurons is given by the binomial coefficient

$$C = \binom{N}{k}, \tag{1.11}$$

where k is the size of the sub ensembles. A bigger k therefore would allow more representations as long as $k < N/2$. On the other hand the energy costs increase with higher k [70]. Also, the overlap between ensembles increases so that representations become more and more redundant [72]. Therefore ensemble size is a balance between energy consumption, possible representations and uniqueness of representations.

Combining the concepts of population code and individual rate coding raises the question of what synchronicity of ensembles looks like. In the AP-count hypothesis individual rate coders define an ensemble when their activity is integrated over a given time window. The temporal-coding hypothesis states that the precise timing of APs is necessary to add information to the AP counts [75]. Whether the coding of neural network is better described by AP-counts or temporal coding is different for individual networks and is also dependent on their proposed function [76].

In order to form representations synaptic connections between computational layers require the ability to adapt to new patterns and stimuli. The property of adaption is called synaptic plasticity.

1.1.5 Plasticity

How is a cell assembly defined and how does it form? In the classical definition, simultaneous activity of cells is equivalent to functional excitatory synapses between those cells [1, 73]. In this so called Hebbian cell assemblies, the simultaneous activity of the n'th input and a given output cell triggers are strengthening of their synaptic connection w_n. A stable description of Hebbian learning is Oja's learning rule

$$\Delta w_n = \eta A_{\text{out}}(A_n - A_{\text{out}} w_n), \tag{1.12}$$

where η is the learning rate [77]. Following this concept, synchronous activity leads to a long-term potentiation (LTP) of the synapse whereas non-synchronicity leads to a long term de-

pression (LTD). Experimentally, Hebbian learning has been shown to describe the plasticity found in real neural networks [78, 79] and was the theoretical starting point for other plasticity mechanisms, such as short-term plasticity and depression (STP and STD), as well as spike time dependent plasticity (STDP).

Plasticity mechanisms depend on synchronous firing. Activity has to be within a certain time window before cells go back to equilibrium, so that potentiation can happen; This sets the timing to a few milliseconds which is in the range of one period of γ-oscillations. The similar time frame for plasticity mechanisms and network oscillations is therefore hypothesized to define the timing and tuning of the synaptic connectivity matrix. This so called "synapsemble" is thought to underlie the formation of cell assemblies and thus to define the syntax of neural code [59].

Competitive learning synapsembles between individual layers are the basis for the formation of memories, which is performed most prominently in the hippocampus [80].

1.2 The hippocampal navigation and memory system

The hippocampus is the brain region responsible for spatial memory and general memory formation [7, 81]. In humans, the hippocampus is deeply embedded into the temporal lobe and has been shown to be crucial for the encoding of new memories [3]. In rats, the discovery of place cells has led to the conclusion that the hippocampus forms a cognitive map and a representation of space [5]. Further, lesion experiments have shown that orientation is highly impaired without the hippocampus [5, 82]. These unique features come along with unique morphological and computational properties.

The hippocampus has two densely packed principal cell layers, the granule cell (GC) layer and the CA pyramidal cell layers, that wrap each other in double-U like fashion [6](see Fig. 1.4). Functionally, the hippocampal circuitry forms a circular mainly unidirectional activity flow between entorhinal cortices and the hippocampus proper (See Fig. 1.5), where the main excitatory input comes the entorhinal area.

1.2.1 Hippocampal inputs

Indirectly, information from all cortical areas reaches the hippocampus. Before reaching it, this information is relayed by the entorhinal cortices that are the main afferent structures to the hippocampus. Medial and lateral entorhinal cortex (MEC and LEC, respectively), though not part of the hippocampus proper, are counted as a part of the hippocampal formation due to the high interconnectivity between these regions. LEC and MEC receive and compute information from different cortical regions before transmitting it to the hippocampus. LEC encodes somatosensory information [83, 84] and projects non-spatial features such as object identity [85] and time [86]. MEC integrates spatial egocentric information from other regions of the cortex [87] and encodes self motion information [88, 89]. The hippocampal projecting neurons from MEC layer II are functionally diverse, combining grid cells, head-direction

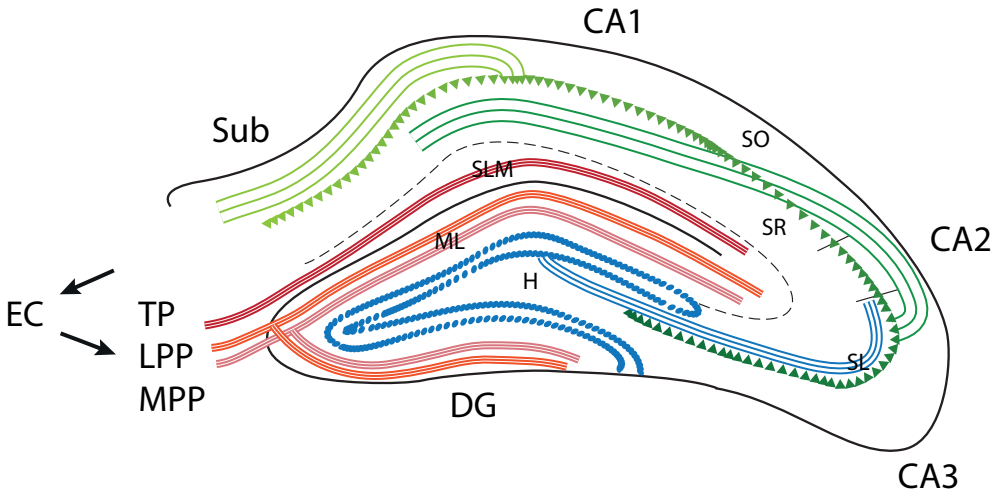

Figure 1.4 – Schematic of the layer structure, locations of principal cells and anoxic connections in the hippocampus proper. DG forms the main input layer of the hippocampus receiving EC projections through the MPP and LPP (pink and red, respectively). Granule cells (blue) send dendrites in the ML and forward activity through mossy fibers into SL of CA3. CA3 pyramidal cells (dark green) receive mossy fiber input as well as direct MPP and LPP input. They form recurrent connections in SR and SO (not shown) and send axons to CA2 and CA1. CA1 pyramidal cells (light green) receive CA3 input in SR and SO and EC input through TP (dark red) in SLM. CA1 is main output structure sending axons to subiculum and deep layers of EC.

cells, and border cells, as well as non-spatial cells [90]. Further, a subset of these cells shows speed-modulated activity that is transmitted to the hippocampus [91, 92]. Both regions show activity in the θ-band, a rhythm also prominent in the hippocampus [55].

The pathways that project from MEC and LEC onto DG and CA3 are called the medial and lateral perforant path (MPP and LPP, respectively) [93]. MPP and LPP fibers originate in layer II of LEC and MEC and terminate in the outer and medial part of the DG molecular layer, respectively, where they innervate GC dendrites (See fig. 1.4)[94]. Further, they form synapses with pyramidal cells in CA3 in stratum lacunosum moleculare (SLM). CA1 pyramidal cells receive input from LEC and MEC through a separate pathway, the temporoammonic pathway, that originates in layer III of the ECs [95].

Additionally to the main pathway of activity, the hippocampus receives modulatory inputs from the medial septum and the diagonal band of broca. These are the key structures that modulate hippocampal rhythmogenesis [51, 52, 96].

The ECs are not only the main input to the hippocampus proper but also its main output targets, thus these regions form a circular connectivity pattern (See Fig. 1.5). This connectivity loop drives the circuitry of the hippocampus proper, which forms the basis for the current understanding of memory encoding.

1.2.2 The dentate gyrus

The dentate gyrus (DG) is the main input layer to the hippocampus, with its sparsely active network of densely packed granule cells (GCs). Its main functional role is to create a sparse

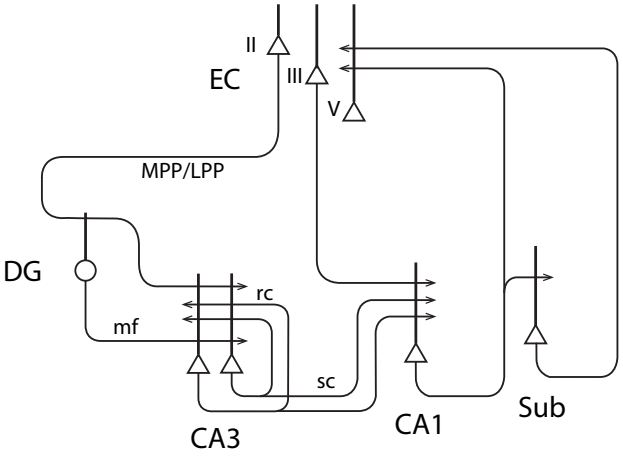

Figure 1.5 – Hippocampal circuit. Layer II EC cells project through MPP and LPP onto DG and CA3. DG is the input layer of the hippocampus where the code is expanded and orthogonalized. GCs have strong projections onto CA3 through mossi fiber (mf) synapses. Most CA3 inputs are recurrent connections (rc) from other pyramidal cells. CA3 forms an attractor network that completes previously leaned patterns from DG inputs. Activity is forwarded through Shaffer collaterals (sc) to CA1 where it is further expanded. CA1 also receives EC input from layer III so that direct input can be compared to CA3 output. CA1 output is send back to EC layer V directly as well as indirectly through subiculum. Modified from [97].

orthogonal representation of inputs from MEC and LEC, the basis of pattern separation.

Granule cells of dentate gyrus

The DG upper and lower blade of GCs wrap the hilus (H) on the inside and are surrounded by the molecular layer (ML) on the outside (See Fig. 1.4). The principal cell layer contains $\sim 500,000$ GCs in young mice, small ovally formed excitatory neurons ($\sim 10\,\mu$m diameter), that send their dendrites into ML [98]. Only 2% to 5% of the GC population is active during an experience [99] and the activity rates of those GCs that are active is very low in the range of 0.1 to 0.5 Hz [100, 101]. Even though GCs generate APs sparsely, approximately two third of APs happen in short bursts with on average three APs per burst at 100 Hz [102, 103]. This sparseness is supported by GC intrinsic properties with a low resting potential of $V_{\text{rest}} \approx 80\,\text{mV}$ in vivo and and in vitro [101, 104] as well as a relatively high threshold for AP generation of $\theta \approx -49\,\text{mV}$ [105] (see eq. 1.4 and 1.6, respectively).

GC dendritic properties of integration and synapse formation play an important role for GC activity and function [106]. GCs do not show boosting effects of inputs, but a strong voltage attenuation and linearized summation of inputs thus leading to an equal impact of individual MPP and LPP synapses [107]. Those synapses show a Hebb-like modifiability and act as a competitive learning network [108]. This network is suitable to remove redundancy from the inputs [109] even with a single exposure to new input [110].

Inhibitory control of granule cells

The sparseness of GC activity is further enhanced via strong inhibitory feed-back and feed forward motifs inside DG [111–113]. These motifs are set up by at least five different classes of interneurons that differ in location, morphology, excitatory drive, targeted cells and cell compartments, electrophysiological properties, and gene expression [114, 115]. Defining for their function in DG circuit motifs is whether the excitatory drive comes from the perforant path (feed forward), the mossy fibers (feed-back), or both. The most studied example of the last group is the fast spiking, parvalbumin expressing (PV^+) basket cell named after its basket

like axonal plexus around the principal cell soma [116–118]. PV^+-cells are thought to mainly inhibit GCs laterally [112]. Another group are hilar commissural-associational path related cell (HICAP), cholecystokinin positive (CCK^+) interneurons that innervate the inner third of the ML [115]. PV^+- as well as CCK^+-cells mediate normalizing inhibition according to formulas 1.9 and 1.10. Typical feed back interneurons are the hilar perforant path associated (HIPP), somatostatin positive (SST^+) interneurons [119]. HIPP cells, like molecular layer perforant path associated (MOPP) cells, terminate at the middle and outer third of the ML. Thus, they directly balance the excitatory inputs at the GC dendrites in accordance with equation 1.4 [115]. A special interneuron type in the DG are the so called mossy cells (MCs) that have an excitatory effect on targeted cells[120]. MCs are located within the hilus and project exclusively inside the DG but all along the sept-temporal axis. Their function inside the DG network is still under debate [40, 121, 122].

Pattern separation

The low excitability of GCs together with competitive learning at DG synapses and a strong inhibitory control sets up the very sparse DG network. This sparseness motivated the theory of DG as a pattern separator [7, 97, 110, 123, 124]. Pattern separation describes the networks ability to create distinct orthogonal representations from overlapping or similar inputs [9, 12]. In order to create a full set of population representations (the coding subspace) of all possible inputs the network needs to contain a high number of principal cells [125], which is given by the high number of GCs in the network. Further, for a de-correlation of the input activity principal cells in the pattern separator need to outnumber the cells of the input network, a concept called "expansion recoding" [7, 126]. Since GCs outnumber the cells of the input network by a ratio of 5:1 [10], the DG network is able to expanse the entorhinal input.

The behavioral correlate of pattern separation lies in the differentiation of two almost similar but not identical environments [8]. It has been shown that animals with an impaired plasticity at GC synapses lack the ability to distinguish subtle spatial differences in a spatial fear conditioning paradigm[127]. Further, the DG also plays a crucial role in detecting the relocation of an object in the so called object pattern separation (OPS) task[128]. The computational mechanism that is supposed to denote that change of environment is a remapping event of GC place code. Whether remapping happens gradually [10] or drastically [129] and whether the DG it is more sensitive local [130] or global spatial cues [131] is still a matter of debate. Generally, the direct correlation of computational orthogonalization and behavioral pattern separation is still not fully understood.

1.2.3 The CA3 region

GC axons (mossy fibers) innervate CA3 in stratum lucidum (SL) and each CA3 pyramidal cell receives ~ 50 mossy fiber inputs [97](See Fig. 1.4). Compared to GCs, pyramidal cells are larger (~ 20 μm diameter) and there are ~ 191,000 pyramidal cells in the young mouse CA3 [98]. Their dendritic trees reach out on both sides of the pyramidal cell layer into stratum radiatum (SR) and stratum oriens (SO) [132]. In these layers CA3 pyramidal cells form and re-

ceive direct recurrent excitatory connections from other CA3 cells, forming an auto recursive network [42].

Mossy fiber synapses have a strong impact on CA3 pyramidal cells so that even single GCs are able to trigger APs [133]. Therefore, GCs they have a significant influence on CA3 activity even though GC activity is sparse and each pyramidal cell receives only ~ 50 mossy fiber inputs. CA3 pyramidal cell number is lower than the number of GCs by a ratio of 1:2.5 [98] which leads to a convergence of activity in CA3 [126]. The majority of CA3 inputs are formed by recurrent excitatory connections from other CA3 pyramidal cells in the range of 10^4 [97]. The probability of these connections follows a scale-free topology, leading to the emergence of so called hub neurons [134]. Such a recurrent excitatory network is called an attractor network [74, 135, 136]. CA3 axons forward activity to afferent CA2 and CA1 pyramidal cells through the so called Shaffer collaterals.

Pattern completion

Attractor networks converge on generalized activity patterns, even when inputs are incomplete ore noisy. This feature is called generalization or pattern completion [137, 138]. A mnemonic representation in the neural network needs to be reliable even if inputs are not sufficient or noisy. Therefore, the memory encoding network needs to perform both tasks, pattern separation and completion [7]. Due to the anatomical differences required for pattern separation and pattern completion one single network cannot perform both tasks but it needs to be separated in layers. Thus, DG and CA3 form the hippocampal layers that together perform both tasks of pattern separation and completion before activity is forwarded to CA1.

1.2.4 The CA1 region

Within CA1 there are ~ 223,000 pyramidal cells [98] and each cell receives input from 15.000 to 30.000 CA3 cells [139]. These synaptic connections are formed in the SR and SO layers of the CA2/1 regions(See Fig. 1.4). In contrast to the CA3 region, CA1 pyramidal cells have only few axon collaterals within in CA1 [132], but project to the subiculum and layer V of the EC [94]. Thus, CA1 is the main output structure of the hippocampus. The discussion of all different interneuron classes in CA layers is beyond the scope if this work but can be found elsewhere [115, 140].

The hippocampal code expands further in CA1 due to the higher number of pyramidal cells compared to CA3 [98] (This contrast is even more pronounced in higher mammals [97]). This code expansion leads to a distribution of the information content from CA3 and provides the first part of the expansion for the return projections to neocortical regions [97]. At the same time a high number of Shaffer collateral terminals converge on each CA1 pyramidal cell where they form a competitive learning network [139, 141]. Together, expansion and conversion create a representation of the same information content as in CA3, but more robust against noise and individual firing levels [97]. Additionally to a full representation, e.g. of space, CA1 encodes sequences in which spatial cues and certain locations appear

[142]. Thus, CA1 is hypothesized to add time information to the representations it receives from CA3 [97]. CA1 does not only receive information from CA3, but also direct EC input through the temporoammonic pathway. This combination of previously computed and direct input enables CA1 cells to compare previously learned and current patterns. Indeed it has been shown that the disruption of the direct EC input to the CA1 subregion of the dorsal hippocampus interferes with spatial working memory and novelty detection [143].

For all of these hippocampal computations most experimental evidence in rodents is found in place coding and during orientation.

1.3 State dependent processing

1.3.1 Place code and stability

One main task of the hippocampus is to form and memorize a representation of space [5]. This spacial map has its direct correlate in place cells (PCs), that rate code distinct places in space, their place fields. PCs are found in all hippocampal layers and show different properties. One defining feature for PCs is how they change their behavior depending on the spatial context. It has originally been shown in CA3 that place cells change their firing field in a different spatial context, a phenomenon referred to as "remapping" [144]. In remapping, PCs can change the position of their place field but also stop or start place coding depending on the context. The degree of remapping for changing contexts in each hippocampal layer reflects its sensitivity or stability to changes in environment. These features are hypothesized to reflect the concept of pattern separation and completion in DG and CA3, respectively. Different theories what this translation looks like are debated, based on different experimental evidences [10, 129–131].

Another question is how place code evolves and facilitates in different layers. Forming of the spatial map is thought to be dependent on the activity state. Especially in the hippocampus different activity states are identified with specific oscillatory patterns [55] and are further linked to stereotypical behavioral states.

1.3.2 State dependence and oscillations

Orientation is differently relevant depending on the behavioral state, especially the difference between locomotion and immobility. It has been shown that already several hundred milliseconds before rodents engage in locomotion, its upcoming onset can be predicted by the emergence of θ-oscillations in the hippocampus [57, 58]. Activity in the θ-band has been shown to be present during all exploratory behaviors, including walking, sniffing and rearing, and the paradoxical phase of sleep [56]. The correlation of θ-rhythm and locomotion is functionally so relevant that an artificial activation of the medial septum, thus triggering θ-activity, is sufficient to induce locomotion [145]. During locomotion, activity of individual cells locks to the phase of the oscillation frequency. This is especially true for place cells, where the synchronization creates an interference pattern known as phase precession [146].

From that interference pattern the distance traveled from the beginning of the place field can be instantly inferred from the theta phase of the place cell spikes [147, 148]. Further, changes in hippocampal θ-synchronization are translated into rapid adjustment of running speed via the lateral septum [149]. Accordingly, CA1 pyramidal neurons almost linearly increase their firing rates with the velocity of locomotion [150–152]. The precision of timing within the theta rhythm is so important that a disruption of it critically impairs the function of the hippocampus [153]. Due to these behavioral correlates, θ-oscillations are believed to be crucial for temporal coding of active neuronal ensembles and the modification of synaptic weights [55]. Thus, theta rhythm plays an important role for spatial learning and the creation of the spatial map [60].

As noted earlier (see section 1.1.3), θ-rhythm often coincides with activity in the γ-band. This is especially true in the hippocampus where γ is hypothesized to set the timing for synchronous ensembles [59]. Indeed approximately 1 % of hippocampal pyramidal cells fire in a 20 ms time window during theta-related behaviors [150]. Considering that 15,000 to 30,000 CA3 pyramidal cells converge on a CA1 pyramidal neuron [139, 141], on average, 150 to 300 CA3 pyramidal cells firing within a gamma cycle comprise an assembly [154].

However, during awake immobility, drinking, grooming, drowsiness, and slow wave sleep θ-activity is replaced by irregular patterns. These include δ-waves, sleep spindles, sharp waves (SPW), and dentate spikes [48, 155]. The behavioral relevance of non-theta related activity is, with SPW as prominent exception, far less studied in the hippocampus. This is especially true in the dentate gyrus.

Despite the general sparseness of GC activity, there are network activity patterns in the DG correlated to different activity states. During locomotion a strong θ-activity is mediated through the MPP and LPP inputs onto the DG [56]. The θ-modulation of entorhinal input to the DG is able to suppress the otherwise very strong inhibitory feed forward mechanisms [111]. The modulated input drive triggers interaction of PV^+ interneurons that is hypothesized to set up the γ-modulation that superimposes θ-rhythm [45]. This γ-modulation of GC output can recruit lateral inhibitory feed-back mechanisms [113]. Even though individual GC activity remains sparse, activity couples to θ- as well as the γ-rhythm [46, 102, 103, 156]. Therefore it is not surprising that GCs show differences in activity whether the mouse is immobile or in locomotion [157].

During immobility synchronized non-rhythmic network events occur in the DG called dentate spikes [155]. Type 1 dentate spikes (DS1) are driven by the LPP projections whereas type 2 spikes (DS2) are driven by the MPP. Dentate spikes activate inhibitory networks in the hilus but suppress activity in efferent regions. However, it is unclear how cellular identity of DS1 or DS2 looks like, due to a lack of studies on the number of recruited cells during dentate spikes and whether activated ensembles are repetitive. Furthermore, it remains unsolved how these network events fit into the picture of DG pattern separation.

1.4 Key questions

So far, studies observing DG function have mainly focussed on animals during locomotion. Only during locomotion hippocampal principal cells reveal one of their main read outs, which is place coding. Thus, activity patterns during immobility are poorly studied especially in DG.

The goal of this thesis is to evaluate DG computations in different behavioral states on a cellular level and to answer the following key questions:

- How does DG compute perforant path input in different states?
- Is network activity observable on a cellular level in DG output, especially when the animal is resting?
- If network phenomena are present, what is the nature of activated ensembles? Is orthogonality preserved in network activity?
- What is the behavioral relevance of DG activity during rest?

Chapter 2

Materials and Methods

2.1 Animals and procedures

All animal experiments were conducted in accordance with European (2010/63/EU) and federal law (TierSchG, TierSchVersV) on animal care and use and approved by the county of North-Rhine Westphalia (LANUV AZ 84-02.04.2015.A524). We used 9-12 weeks old Thy1-gCaMP6 mouse line (GP4.12Dkim/J) mice for imaging experiments, which express gCaMP6s in most hippocampal neurons [158]. In total $n = 10$ animals were used for experiments.

2.1.1 Virus injections and head fixation

Thy1-gCaMP6 mice were anesthetized with a combination of fentanyl /midazolam /medetomidine (0.05/5.0/0.5 mg/kg body weight i.p.) and head-fixed in a stereotactic frame. 30 min prior to induction of anesthesia, the animals were given a subcutaneous injection of ketoprofen (5 mg/kg body weight). Eyes were covered with eye-ointment (Bepanthen, Bayer) to prevent drying and body temperature was maintained at 37°C using a regulated heating plate (TCAT-2LV, Physitemp) and a rectal thermal probe. After removal of the head hair and superficial disinfection, the scalp was removed about 1 cm^2 around the middle of the skull. The surface was locally anesthetized with a drop of 10 % lidocaine and after 3-5 min residual soft tissue was removed from the skull bones with a scraper and 3 % H_2O_2/NaCl solution. After complete drying, the cranial sutures were clearly visible and served as orientation for the determination of the drilling and injection sites. For virus injection, a hole was carefully drilled through the skull with a dental drill, avoiding excessive heating and injury to the meninges. Any minor bleeding was stopped with a sterile pad. The target site was located as the joint of Parietal, Interparietal and Occipital skull plates. Subsequently, the tip of a precision syringe (cannula size 34 G) was navigated stereotactically through the burrhole (30° towards vertical sagittal plane, 1.5 mm depth from skull surface) and virus particles (rAAV2/1-CaMKIIa-NES-jRGECO1a [159]) were slowly injected (total volume 250 nl, 50 nl/min) in the medial entorhinal cortex. Correct injection site in the medial entorhinal cortex was verified in all cases by confined expression of jRGECO1a in the middle molecular layer of the dentate gyrus (Fig.

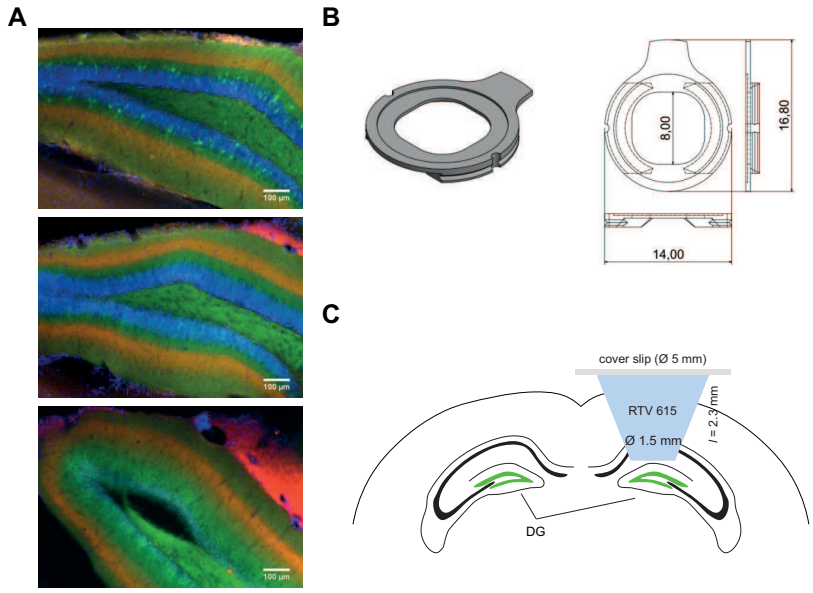

Figure 2.1 – Preparation of experimental animals. A, histological preparations of Thy1-gCaMP6s animals injected with jRGECO in MEC. 70 μm fixed slices of DG with DAPI stained nuclei (blue), gCaMP6s (green) and jRGECO (red) (n = 3). B, custom made head fixation plate made from AL. Design is flat on the skull with notches for the fixation holder going down on both sides on the skull. Handle on the back allows handling, habituation and mounting in the set up. C, 2D view of position and size of the cone shaped silicon inset. The window is inserted after aspiration of cortical and CA1 tissue above DG.

2.1A). To prevent reflux of the injected fluid, the cannula was retained for 5 minutes at the injection site. Optibond (OptibondTM 3FL; two component, 48 % filled dental adhesive, bottle kit; Kerr; FL, USA) was then applied thinly to the skull to aid adhesion of dental cement. Subsequently, a flat custom made head post ring (Fig. 2.1B) was applied with the aid of dental cement (Tetric Evoflow), the borehole was closed and the surrounding skin adapted with tissue glue, also closing the borehole and adapting the surrounding skin with tissue glue. At the end of the surgery, anesthesia was terminated by i.p. injection of antagonists (naloxone /flumazenil /atipamezole, 1.2/0.5/2.5 mg/kg body weight). Postoperative analgesia was carried out over three days with once daily ketoprofen (5 mg/kg body weight, s.c.).

2.1.2 Window implantation procedure

Cranial window surgery was performed to allow imaging from the hippocampal dentate gyrus two weeks after virus injection. 30 minutes before induction of anesthesia, the analgesis buprenorphine was administered for analgesia (0.05 mg/kg body weight) and dexamethasone (0.1 mg/20 g body weight) was given to inhibit inflammation. Mice were anesthetized with 3-4 % isoflurane in an oxygen/air mixture (25/75 %) and then placed in a stereotactic frame. Eyes were covered with eye-ointment (Bepanthen, Bayer) to prevent drying and body temperature was maintained at 37°C using a regulated heating plate (TCAT-2LV, Physitemp) and a rectal thermal probe. The further anesthesia was carried out via a mask with a reduced isoflurane dose of 1-2 % at a gas flow of about 0.5 l/min. A circular craniotomy (diameter 3 mm) was opened above the right hemisphere hippocampus using a dental drill. Cortical and CA1 tissue was aspirated using a blunted 27-gauge needle until the blood vessels above the dentate gyrus became visible. A custom made cone-shaped silicon inset (Upper diameter 3 mm, lower diameter 1.5 mm, length 2.3 mm, RTV 615, Movimentive) attached to by a cover glass (diameter 5 mm, thickness 0.17 mm) was inserted and fixed with dental cement.

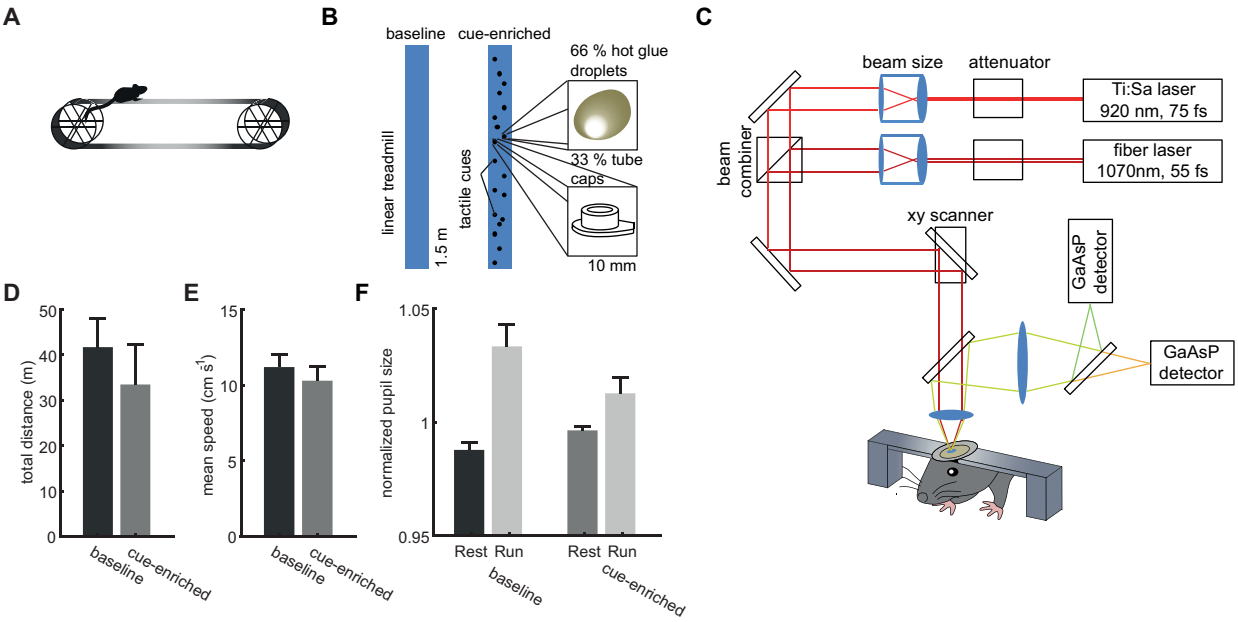

Figure 2.2 – Two photon imaging in behaving mice on linear treadmill. A, concept of custom made linear treadmill. B, belt design for 1.5 m long blank belt (left) as well as cue enriched belt (right). C, Light path for two photon scanning microscopy. Two excitation light paths are implemented at 920 nm and 1070 nm to excite green and red floruphores. x-scanning is done by a resonant galvanometric scanner, y-slow-axis-scanning by a galvanometric scanner. Photon section is done for two chromatically separated channels using gated GaAsP detectors. D, running distance per session was 40 m mean in both empty belt and cue-enriched belt. E, mean running speed was 10 cm/s in both conditions. F, pupils size of immobile and locomotion periods on blank and enriched running belts.

This special window design allowed easy implantation and maintenance and minimized the amount of aspirated tissue. Further the geometry was optimal for conserving the numerical aperture of the objective (Fig. 2.1C). Postoperative care included analgesia by administering buprenorphine twice daily (0.05 mg/kg body weight) and ketoprofen once daily (5 mg/kg body weight s.c.) on the three consecutive days after surgery. Animals were carefully monitored twice daily on the following three days, and recovered from surgery within 24-48 hours, showing normal activity and no signs of pain. The preparation of CA1 imaging windows followed mainly the same protocol. Here only the cortex was aspirated until the alveus fibers above CA1 became visible. The silicon inset was a shorter version (length 1.5 mm) of the one used for DG experiments. We have tested the functionality of our head fixation and window design in a former study [160].

2.2 Linear treadmill system

The treadmill we implemented was a self-constructed linear horizontal treadmill, similar to [33] (see Fig. 2.2A). The belt ran over 3D-printed wheels on each end of the treadmill and kept in position under the objective with a restrainer bill from teflon plates. The designed holder for the head fixation kept the mouse head in position under the objective. To adjust

for the size of each animal and the optimal angle for imaging the holder was mounted on an adjustable stage (L200M, Thorlabs, USA) and a two axis goniometer (GNL20M, THorlabs, USA), respectively. The complete apparatus was installed on a moveable shifting table (380 FM-U, Luigs und Neumann, Germany) and fitted to a commercial microscope (A1 MP, Nikon, Japan). The belt surface was either left blank or equipped with tactile cues (Fig. 2.2B). Belt position and running speed were measured by modified optical mouse sensors installed at the back-wheel and controlled by an Arduino micro controller (Arduino Uno, Arduino AG, Italy). Stimulation hardware was controlled using a Tinkerforge Masterbrick micro controller (Tinkerforge GmbH, Germany). All behavioral recordings were synchronized at a recording frequency of 100 Hz and later sampled down to match the imaging frame rate. All stimulation and acquisition processes were controlled by custom-made software written in LabView (National Instruments Corporation, USA).

2.2.1 Habituation and behavior on the linear track

Experiments were performed in head-fixed awake mice running on a linear track. Two weeks before the measurements, mice were habituated to the head fixation. Initially, mice were placed on the treadmill without fixation for 5 minutes at a time. Subsequently, mice were head-fixed, but immediately removed if signs of fear or anxiety were observed. These habituation sessions lasted 5 minutes each and were carried out three times per day, flanked by 5 minutes of handling. During the following 3-5 days, sessions were extended to 10 minutes each. After habituation, mice ran well on the treadmill for average distances between 30-40 m per session (Fig. 2.2D) at a mean speed of ~ 10 cm/s (Fig. 2.2E).

2.2.2 Pupil diameter measurement and analysis

On the linear track, the pupil diameter was measured using a high-speed camera (Basler Pilot, Basler, Germany) at a frame rate of 100 Hz. To estimate pupil diameter, a circular shape was fitted to the pupil using the LabView NI Vision toolbox (National Instruments), providing a real-time readout. Post-hoc, the pupil-diameter trace was normalized to its mean. As in a published study [161], frames in which pupil diameters could not be obtained due to blinking or saccades were removed from the trace. The pupil diameter trace was filtered using a Butterworth low-pass filter at a cutoff frequency of 4 Hz. To match the time resolution of the imaging data, the pupil-trace was down-sampled to 15 Hz. Average pupil diameters were calculated for entire episodes of locomotion, entire periods of immobility, and for the single frame coincident with the peak of granule cell activity during network events. Generally, the size of the pupil was more contracted when animals were immobile compared to locomotion states (Fig. 2.2F).

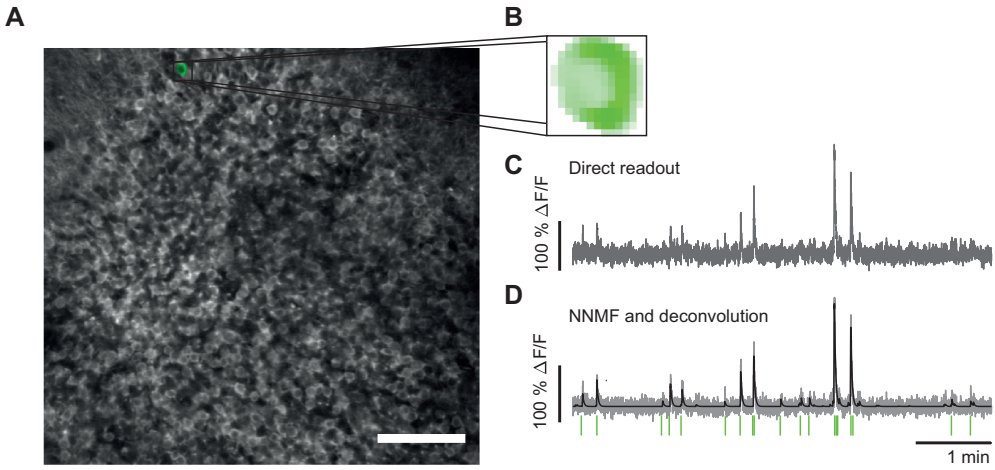

Figure 2.3 – Detection of cells and read out of Ca^{2+} activity traces. A, field of view in a representative session. Greyscale of several hundred GCs in the DG cell layer stained with gCaMP6s in their cytosol. Scalebar = 100 μm. B, spatial footprint of an identified GC using NNMF. C, $\Delta F/F$-trace red out from the area of the identified cell using conventional read out methods. D, same $\Delta F/F$-trace as in B identified with NNMF (Grey line). Deconvoluted de-noised trace of activity (black line) and identified events onsets (green vertical lines).

2.3 Two-photon calcium imaging

For two photon imaging we adapted a standard configuration [162] of excitation and emission light path (Fig. 2.2C). We used a commercially available confocal microscope (A1 MP, Nikon, Japan) equipped with a 25X long-working-distance, water-immersion objective (N.A. = 1, WD = 4 mm, XLPLN25XSVMP2, Olympus) controlled by NIS-Elements software (Nikon, Japan).
gCaMP6s was excited at 940 nm using a Ti:Sapphire laser system (~ 60 fs) laser pulse width; Chameleon Vision-S, Coherent, Ireland). An additional fiber laser system at 1070 nm (55 fs laser pulse width, Fidelity-2, Coherent, Ireland) was added to the setup to excite jRGECO1a. Emitted photons were collected using gated GaAsP photomultipliers (H11706-40, Hamamatsu, Japan). Movies were recorded using a resonant scanning system at a frame rate of 15 Hz and duration of 20 minutes per movie.

The setup was equipped with two additional diode pumped solid state laser systems at 488 nm and 561 nm, respectively. The lasers could be used as excitation light sources for light sensitive opsins [163]. Though this setup configuration was not used for this study, we had used it for a former study that proved the *in-vivo* function of the optogenetic silencer PAC-K [160].

2.4 Data analysis of imaging data

All analysis on imaging data and treadmill behavior data were conducted in MATLAB using standard toolboxes, open access toolboxes and custom written code. To remove motion artifacts, recorded movies were registered using a Lucas-Kanade model [164]. Individual cell

fluorescence traces were identified and Ca^{2+} events were deconvolved using a constrained non-negative matrix factorization based algorithm [165]. All components were manually inspected and only those kept that showed shape and size of a granular cell and at least one significant Ca^{2+}-event in their extracted fluorescence trace. We binarised individual cell fluorescence traces by converting the onsets of detected Ca^{2+} events to binary activity events.

MPP input bulk signal was analyzed by setting a region of interest in the molecular layer. For that a threshold of 50 % maximum fluorescence was used within the field of view on the average projection of the movie. The bulk fluorescence signal trace was calculated as the average signal of the defined region of interest in each frame. The baseline for the bulk signal was defined as the low pass filtered signal of the raw trace with a cutoff frequency of 0.01 Hz using a Butterworth filter model.

Cross correlation analysis between MPP and GC signals were conducted with standard Matlab routines. For Granger causality testing a special toolbox was used (Chandler 2020. Granger Causality Test, MATLAB Central File Exchange).

2.4.1 Network activity

To define network events (NEs) of synchronized activity we first searched for Ca^{2+}-event onsets occurring simultaneously within a moving time window of 200 ms (3 frames). We then defined the distribution of synchronous events that could arise by chance in each individual session. To achieve this, all individual onset times were randomly shuffled and the resulting number of NEs from the shuffled traces were calculated. We repeated that process a thousand times to create a null-distribution for chance level of NEs. We set the minimal threshold for network events in each individual session at a number of cells where less than 0.1 % of events ($p < 0.001$) could be explained by chance.

Orthogonality between pairs of network events was assessed using cosine-similarity measures $S_{\cos}$. Population vectors $v_{\text{net},i}$ of all network events were multiplied using the normalized vector-product in a pair-wise manner:

$$S_{\cos} = \frac{v_{\text{net},i}\, v_{\text{net},j}}{|v_{\text{net},i}||v_{\text{net},j}|} \tag{2.1}$$

To test which fraction of orthogonal pairs could be explained by chance, we generated a null distribution by randomly reassigning the cell participations to different population vectors a 1000 times. We then tested the real fraction of orthogonal pairs against the fraction derived from the shuffled data.

2.4.2 Spatial tuning

To address spatial tuning of activity in sparsely coding GCs we used spatial tuning vector analysis [166]. We restricted analysis to running epochs, where a running epoch was defined

as an episode of movement with a minimal duration of 2.5 s above a threshold of 4 cm/s in a forward direction. Only cells with 4 or more event onsets during running epochs were included in the analysis. The belt was divided in 150 evenly sized bins of 1 cm. To take the circular design of the treadmill into account we used polar coordinates to describe positions on the belt. An angle α_i was assigned to every running related event and weighted by the amount of time the animal spend at that position T_i. The spatial tuning vector v_{space} was then defined as the sum of all weighted event angles

$$v_{\text{space}} = \sum_{i}^{J} \left(\frac{\alpha_i}{T_i} \right) \tag{2.2}$$

To balance this vector it was normalized by the total number of running related events J and with the average time per event spend in locomotion and got:

$$v_{\text{space}} = \frac{1}{J} \sum_{i}^{J} \left(\frac{T_i}{J} \right) \sum_{i}^{J} \left(\frac{\alpha_i}{T_i} \right) \tag{2.3}$$

We addressed statistical significance by creating the null distribution for every spatially tuned cell. This was achieved by randomly shuffling the onset times and recalculating the spatial tuning vector 1000 times. The p value was calculated as the percentage of vector lengths arising from the shuffled distribution that was larger than the actual vector length.

2.4.3 Velocity tuning

To analyze speed modulated activity of GCs, velocity values were divided in 20 evenly sized bins between 0 and the maximum velocity of the animal. We calculated the mean $\Delta F/F$ at all times the animal was running at velocities within each specific velocity bin. Putative speed cells were those granule cells that showed a Pearson's r of at least 0.9. To further exclude the possibility that correlations arise by chance we shifted the individual $\Delta F/F$ traces with respect to the behavior randomly in the time domain a 1000 times. The cell was considered a significant speed coder if the shuffle-data r-values were below the original one in at least 95 % of the cases.

2.4.4 Hierarchical cluster analysis

To find ensembles of correlated activity within network activity, we focused only on those granule cell Ca^{2+} events that occurred within network events. We calculated the correlation matrix using Pearson's r for all cell combinations (Fig. 2.4A). To identify clusters of correlated cells we used agglomerative hierarchical cluster trees (Fig. 2.4B,C). Clusters were combined using a standardized Euclidean distance metric and a weighted average linkage method. Clusters were combined until the mean of the cluster internal r-value reached a

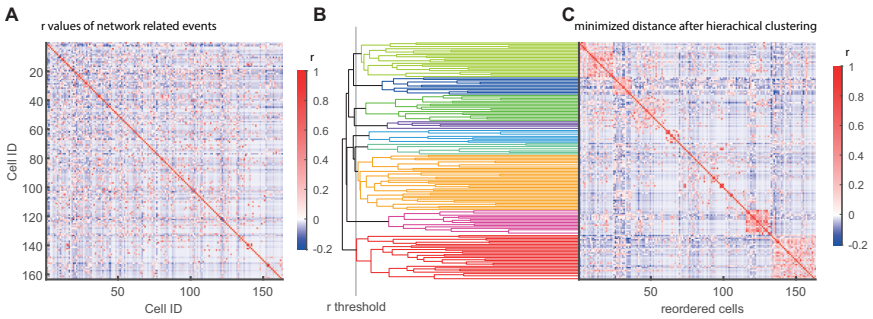

Figure 2.4 – Hierarchical clustering of correlations within network events. A, Correlation matrix with color coded r-values of all cell pairs. Only activity during NEs is used for r-value calculation. B, Agglomerative hierarchical cluster tree using the standardized Euclidean distance metric. Significance threshold is derived from shuffle analysis and color coded are the identified clusters. C, Reordered correlation matrix from A using the identified cluster order from B.

significance threshold. To define the significance threshold we created a null-distribution of r-values from randomized data sets. Data was shuffled by randomly reassigning individual cell events to different network events a 1000 times. The 95 percentile of the created r-value null-distribution was used as the threshold for the clustering procedure. Only clusters in which the mean r-value exceeded the threshold obtained from the null distribution were considered for further analysis.

2.4.5 Principal Component Analysis

To perform Principal Component Analysis (PCA) and Independent Component Analysis (ICA) we used standard MATLAB procedures and calculated the maximal number of components. Gaussian Process Factor Analysis (GPFA) was conducted using a formerly described procedure and toolbox [167], that we adapted for Ca^{2+}-imaging data. Principals were calculated using singular value decomposition (SVD) of the data X of size N by T, where N is the number of cells, T the number of recorded frames and the rows of X are the z-scored $\Delta F/F$ traces, decomposing the data-matrix as

$$X = VW \tag{2.4}$$

where V is an orthogonal matrix whose columns are the principal components, and W is a matrix of associated weights. For an analysis of population activity patterns relative to spatial location, we projected the animal position onto PCA trajectories, allowing us to identify loops in component space reflecting complete rounds on the belt. Further, we projected all individual component amplitudes onto the position of the mouse to detect repetitive patterns. This analysis had comparable results for PCA, as well as ICA and GPFA.

For further analysis we restricted the number of components so that 50 % of variance in each individual data set was explained. To compare running and network related epochs we calculated principal components V_{run} and V_{net} independently from each other so that

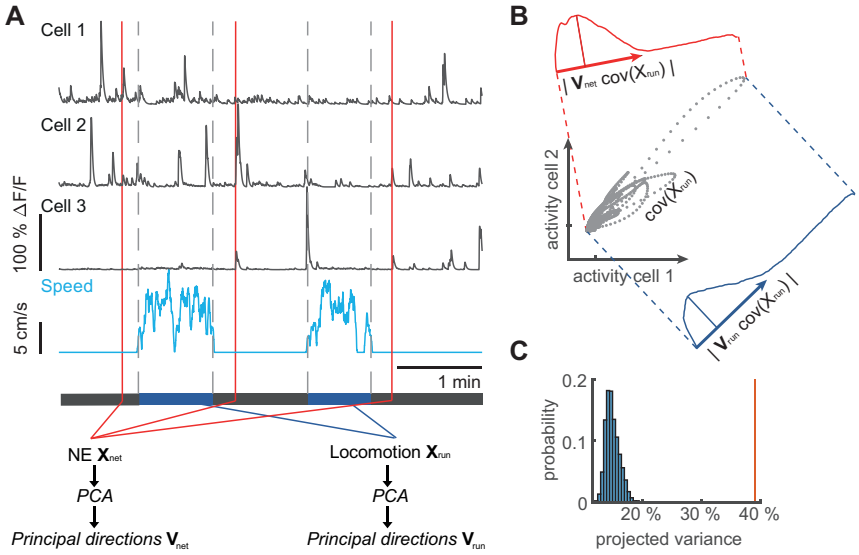

Figure 2.5 – A, schematic of the procedure for comparing population activity during NEs and locomotion. Population activity is represented by 3 cells (upper traces), recorded during running and immobility (blue trace indicates speed). Time point of three network events is indicated schematically by red lines. Activity during NEs was used to perform PCA, computing the transformation matrix V_{net}. Similarly, PCA was performed on the neuronal population activity only from running periods (speed indicated in blue, bordered by vertical grey dashed lines), to generate the transformation matrix V_{run} representing the covarying activity during locomotion. B, Schematic description of the procedure for projecting co-variances of running activity into the PCA basis of network events (or shuffled data). Grey dots show covarying activity of two cells during running. The blue graph denotes the projection into the locomotion PCA-space using V_{run} and the width of the distribution shows the projected variance. The red graph shows the same information for the network space using V_{net}. C, Shuffle analysis. The vertical red line indicates the projected variance explained normalized to original variance. The variance explained is larger than the shuffled distribution (blue), indicating that the population activity during locomotion and network events is more similar than expected by chance (i.e. for network activity without correlations).

$$X_{\text{run}} \approx V_{\text{run}} W_{\text{run}}\,, \quad X_{\text{net}} \approx V_{\text{net}} W_{\text{net}}\,, \tag{2.5}$$

where X_{run} contains all the data from epochs of running and X_{net} the data from 2 s windows around all network events (Fig. 2.5A). To calculate the similarity between these two bases, the covariance of X_{run} was projected into the principal space of the network activity

$$S_{\text{net}\times\text{run}} \approx V_{\text{net}}^{T} \text{Cov}(X_{\text{run}}) V_{\text{net}} \tag{2.6}$$

where $S_{\text{net}\times\text{run}}$ is the matrix of projected co-variances and trace$(S_{\text{net}\times\text{run}})$ quantifies the amount of projected co-variance (Fig. 2.5B). This number was normalized to the total amount of co-variance of locomotion activity in the locomotion principal space trace$(S_{\text{run}\times\text{run}})$.

To compare our results against chance level, we used all traces recorded during immobility, shuffled those with respect to each other in the time domain. We used the original network

times to create a random principal direction space V_{rand} and calculated the projected covariances of X_{run} into the random-network space as trace($S_{\text{rand}\times\text{run}}$) and repeated this procedure 1000 times. The p-value was calculated as the percentage of random projections that exceeded the initial value (Fig. 2.5C).

Additionally, we used two alternative approaches to quantify similarity between the PCA bases. First a similarity factor S_{PCA} as described by [168]:

$$S_{\text{PCA}} = \text{trace}(V_{\text{net}}^T V_{\text{run}} V_{\text{run}}^T V_{\text{net}}) = \sum_{i=1}^{k} \cos^2 \theta_i \,, \tag{2.7}$$

where θ_i is the angle between the i'th principal directions of V_{run} and V_{net}. Further, the Eros similarity factor as described in [169] was used:

$$\text{Eros} = \sum_{i=1}^{k} w_i |\cos \theta_i| \tag{2.8}$$

where w_i is a weighting factor that takes into account the amount of variance that was covered by each individual component. All measures delivered comparable results as compared to shuffled data.

Chapter 3

Results

3.1 Two photon imaging of DG input-output activity

To investigate the output of the DG *in vivo* we imaged the activity of > 300 granule cells (GCs) using a Thy1-gCaMP6s mouse line (GP4.12 Dkim/J [158], $n = 9$ mice). In addition, we monitored the activity of the major input system into the dentate gyrus, the medial perforant path (MPP). To this end, we expressed the red-shifted Ca^{2+} indicator jRGECO1a [159] in the medial entorhinal cortex using viral gene transfer (Fig. 3.1A, B, $n = 4$ mice). To allow efficient excitation of both genetically encoded Ca^{2+} indicators, we established excitation with two pulsed laser sources at 940 nm and 1070 nm. Mice were placed under a two photon microscope and ran on a custom made linear track (Fig. 3.1B, Fig. 2.2, see section 2.3). For Thy1 mice with double staining ($n = 3$) the field of view (FOV) was chosen to cover the GC layer as well as the complete molecular layer so that GC and MPP activity could be monitored simultaneously (Fig. 3.1A lower panel). Without the MPP staining ($n = 6$) the FOV was chosen, so that it covered most of the GC layer (Fig. 2.2A). For the mouse without gCaMP6s expression ($n = 1$) the FOV was set centered around the molecular layer.

The $\Delta F/F$ traces and precise Ca^{2+}-event onset times for each individual GC was read out using non-negative matrix factorization [165](NNMF, see section 2.4). As previously described, the event rate of GCs was generally sparse [131, 157, 166, 170], both when animals were immobile and running on a textured belt without additional cues (mean event frequency 1.38 ± 0.19 events/min and 0.97 ± 0.2 events/min, respectively, $n = 9$ mice, Fig. 3.1E-G). In contrast to previous studies [166], the event rate was higher during immobility (Fig. 3.1E,G), while the mean $\Delta F/F$ amplitude was higher during locomotion. This is most likely caused by our binary definition using only the onset of an event independently from its amplitude and the fact that we considered all cells that showed at least one significant Ca^{2+}-event. Of all GCs, 95 % had activity levels below 4 events/min both during locomotion and immobility, where 57 % did not have any significant events during locomotion (See Fig. 3.1G). During locomotion, even though the fraction of higher active GCs was generally very low, there were more cells in a range above 7 events/min (See Fig. 3.1G inset). This suggests that very sparse GCs had their events preferably during immobility, while higher active cells were more active

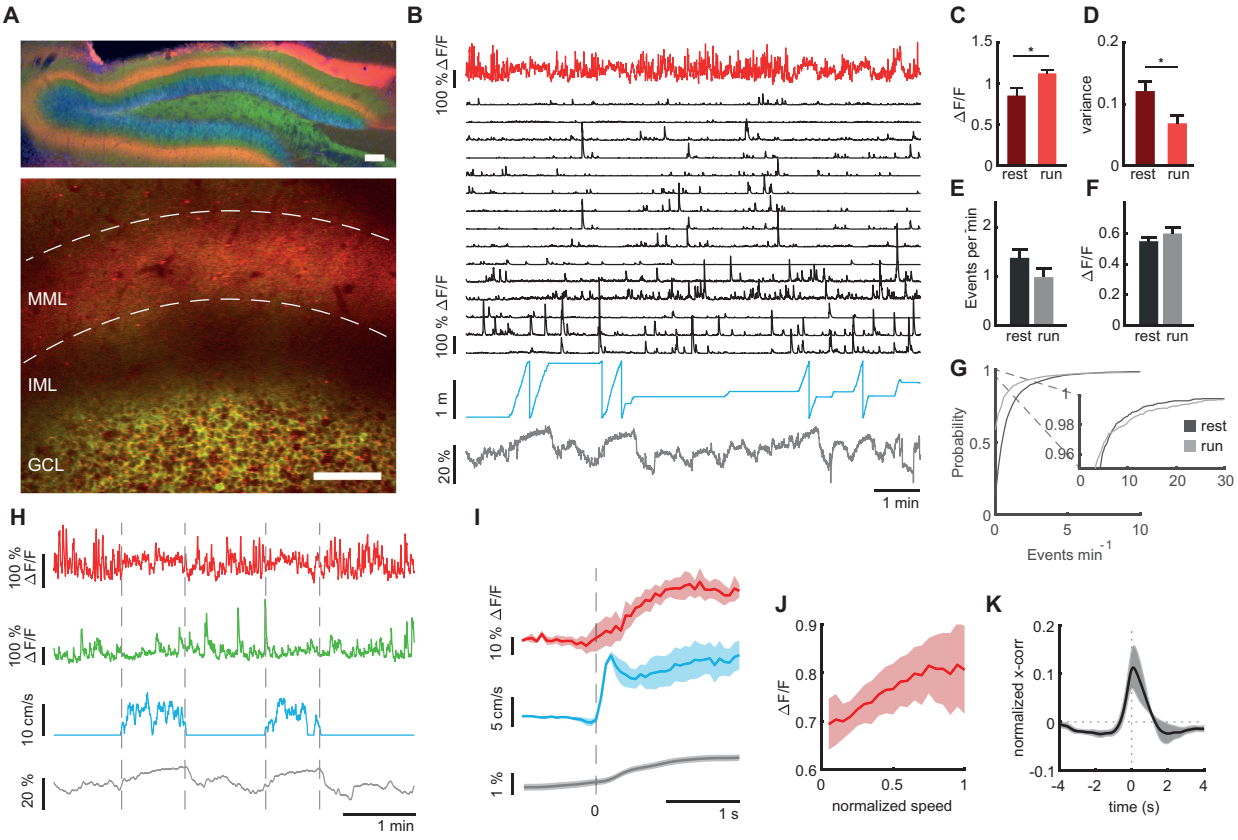

Figure 3.1 – Dual color two photon Ca^{2+}-imaging in awake behaving animals. A upper panel, fixed coronal 70 μm slice of an experimental Thy1 animal injected with jRGECO1a in MEC. Somata are stained with DAPI (blue), GC cytosols are filled with gCaMP6s (green), MPP fibers express jRGECO (red) (Scalebar = 100 μm) . A lower panel, in vivo FOV of the same animal in horizontal view through window implant using the same color code. Scalebar = 100 μm. B, Representative data of one session. MPP bulk signal (red trace) is red out as the sum of all pixels in the middle ML. Individual GC traces (black traces) are red out using NNMF. Speed and position of the animal (blue trace) are red out from the treadmill system. Pupil size (Gray trace) is red out with a high speed camera. C, Mean amplitude of MMP bulk signal during running and resting periods ($n = 4$). D, Mean variance of MMP bulk signal during running and resting periods ($n = 4$). E, Mean GC Ca^{2+}-event frequencies during running and resting periods averaged over mice ($n = 9$). F, Mean GC Ca^{2+}-event amplitudes during running and resting periods averaged over mice ($n = 9$). G, Cumulative probability of GC Ca^{2+}-event frequencies during running and resting periods. The inset shows a close up of the asymptotic tail of the distribution. H, Subset from data from B showing the MPP bulk signal (red trace), the summed GC signal (green trace), the speed of the animal (blue trace) and the pupil diameter (gray trace). I, Averaged data for running onset times showing the MPP bulk activity (red trace), the running speed (blue trace) and the pupil diameter ($n = 3$ mice). 0 is the time of the running onset. J, Mean correlation between the normalized running speed and the normalized MPP fluorescence over experimental animals ($n = 4$). K, cross-correlogram denoting the cross correlation between MPP-bulk signal and summed GC signal.

during locomotion.

The MPP Ca^{2+}-bulk signal was on average higher during locomotion compared to immobile periods (Fig. 3.1C paired t-test, $p = 0.04$, $n = 4$ mice). This increase of fluorescence signal during onsets of locomotion was systematic for all times of locomotion-initiation (Fig. 3.1I). Generally, we found a correlation between MPP-signal amplitude and running speed (Fig. 3.1J), as previously described for MEC cell types[91, 92]. Notably, even though the MPP activity was generally lower during immobility, the MPP activity levels during these phases showed transient, large fluctuations that were only rarely present during locomotion (Fig. 3.1B, H). This was further reflected in a higher variance of the signal during immobility compared to locomotion (Fig. 3.1D paired t-test, $p = 0.03$, $n = 4$ mice).

Cross-correlation revealed that during immobility the increases in MPP activity were associated with peaks in average GC activity levels (Fig. 3.1K). Both signals were significantly correlated in most sessions for periods of immobility (8/9 sessions, Granger causality test $p < 0.05$), but not when the animals were running (8/9 sessions, Granger causality test $p > 0.05$, see section 2.4). This finding suggests that the MPP may contribute to driving synchronized activity in the GC population during immobility.

3.2 Place- and speed-coding granule cells in DG

We identified the properties of GCs, and asked if they encode specific spatial or locomotion-related information on a textured belt without cues as in Fig. 3.1. We first identified GCs that displayed significant position-related firing by calculating significant place preference vectors as previously described [166](Fig. 3.2A for representative polar plots of three GCs, see section 2.4.2). Of the total number of granule cells, a small subgroup of GCs exhibited significant place coding (2.15 %), with place fields distributed over the linear track (Fig. 3.2B). The fraction of place coding cells was lower as reported values [131, 166], since in baseline recordings the spatial environment was sparse. If the fraction of place-coding cells was calculated as a fraction of only GCs active during running as in former studies, the fraction of significantly place-coding GCs was 23 % comparable to previously reported values [166].

Secondly, we identified a fraction of GCs (2.17 %) displaying a significant correlation of activity with running speed (Fig. 3.2C-E, see section 2.4.3). This is in contrast to previous studies [157, 166], but consistent with data obtained in freely moving mice [171]. Notably, we did not observe both speed coding and place coding in the same cells, but in two distinct sub groups of GCs.

The low fraction of PCs was consistent for all three baseline recordings, so we asked whether an enrichment of the spatial environment would induce more pronounced place coding in the GC population. To this end, we increased the density of sensory cues on the textured belt (cue-enriched condition, see section 2.2, Fig. 2.2) in consecutive imaging sessions. In the cue-enriched condition, GC event rate had a trend towards higher frequencies which was not significant (3.2C) while the mean amplitude of events remained unaltered (3.2D).

Indeed we found that place cells were more commonly detected in the cue-enriched condi-

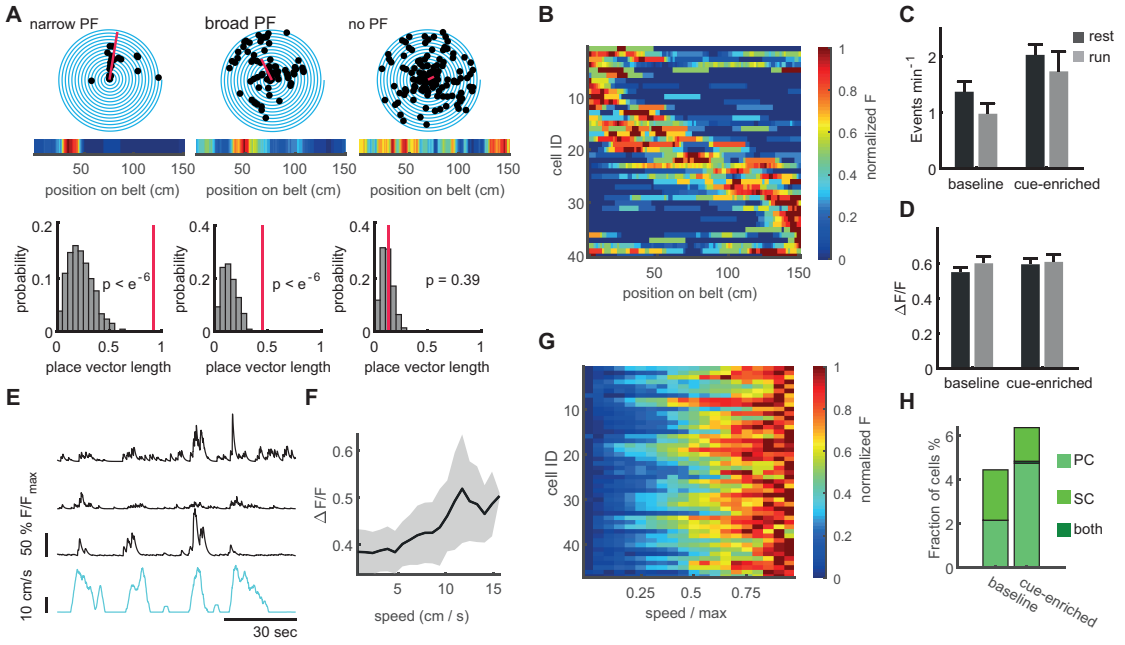

Figure 3.2 – Place and speed cells in the DG. A, Three representative examples of two significantly place-coding granule cells, and one without place coding. Upper three panels show polar plots of the animal position in every round (blue spiral) where each 360° turn of the spiral represents a transition through the 1.5 m linear track. Black dots denote event onsets during locomotion and the red line represents the place vector. The corresponding heatmap of normalized fluorescence is shown in the inset. In lower panels, the distributions for place vector lengths generated from shuffled data are shown (grey histograms), the place vector for the individual cell is indicated as red line. B, Place field heatmaps of all cells showing significant place preference. C, Frequencies of GCs during immobility and locomotion in baseline and cue enriched condition. There is a trend towards higher events frequencies in cue-enriched condition ($n = 9$). D, Amplitudes of events remain unaltered in baseline and cue-enriched condition. E, Representative examples of three significantly speed-coding neurons (black traces, running speed depicted in cyan). F, Speed-modulated mean fluorescence signal of a representative example cell. Gray area indicates standard error. G, Mean fluorescence signals of all significantly speed-modulated cells. Normalized fluorescence is color coded and running speed is normalized to every individual mouse maximum running speed. H, Fraction of place and speed cells on baseline and cue-enriched belts. Number of SCs remains constant whereas the number of PCs has a trend towards higher numbers. There is no overlap between both groups in baseline condition and exactly one cell having both features in cue-enriched condition.

tion (4.66% vs. 2.15% of GCs), while there was no significant change in the proportion of speed cells (2.17% vs. 1.7% of GCs in the baseline and cue-rich conditions, respectively, ^{2}-test regarding changes in the fraction of place and speed cells $p = 6 \times 10^{-4}$, post-test: place cells baseline vs. cue-enriched $p = 1.7 \times 10^{-4}$, speed cells baseline vs. cue-enriched $p = 0.33$, Fig. 3.2H).

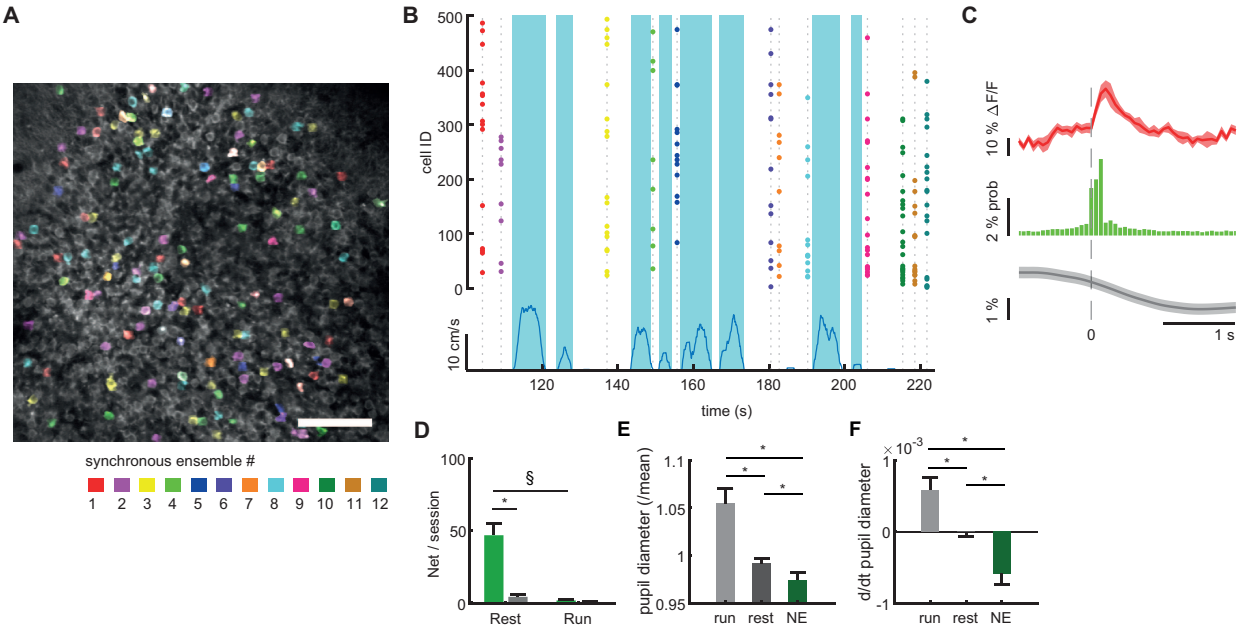

Figure 3.3 – Network events in immobile animals. A, Ensembles of co-active GCs. Every ensemble is color coded with an individual color. Scalebar = 100 μm. B, raster plot of indicted NEs using the same color code from A. Every dot denotes the event onset of an individual cell at NE times. Running speed is additionally shown (blue trace, lower panel) to mark time intervals of locomotion (blue shaded areas). C, Activity averaged around the event times of identified network events (0 is the time of NE) showing MPP bulk signal average (red trace), mean probability for GC events (green bars) and the pupil diameter (gray trace) ($n = 3$ mice). D, Mean rate of NEs per session for running and resting periods (Green bars). Data is shuffled to create a null-distribution for the quantification of random networks (gray bars). E, Mean pupil diameter during running (dark gray), resting (gray) and network events (green bar)($n = 6$). F, Mean derivatives of the pupil diameter during running (dark gray), resting (gray) and network events (green bar)($n = 6$).

3.3 Sparse, structured DG network events in immobile animals

Despite the sparse activity of granule cells, we observed synchronized activity patterns. To rigorously define such events, we used an algorithm that detects synchronized network events within a 200 ms time window (see section 2.4.1). Such synchronous network events could readily be observed in the dentate gyrus (Fig. 3.3). Network events were sparse, incorporating only 5.7 ± 0.09 % of the active GC population.

Notably, network events occurred mainly during immobility and were much less prevalent during running (Fig. 3.3B, D). Shuffling analysis (see section 2.4.1) confirmed that network events do not arise by chance (Fig 3.3D, grey bars correspond to shuffled data, ANOVA $F_{(3,25)} = 30.12$, $p = 4 \times 10^{-14}$, Bonferroni post-test resting vs. shuffled $p = 2.2 \times 10^{-10}$ indicated with asterisk, running vs. shuffled $p = 1$).

As previously described ([161, 172]) we found pupil constriction during immobility with dilation at locomotion onsets (Fig. 3.1H, I). Intriguingly, the average pupil diameters during network events were significantly more constricted compared to the average pupil diameters

during entire periods of immobility (Fig. 3.3E, repeated measures ANOVA for all three groups $F_{(2,28)} = 17.17$, $p = 1 \times 10^{-5}$, $n = 6$, data from 3 sessions each, Bonferroni post tests: pupil diameters during locomotion vs. immobility $p = 0.007$, locomotion vs. network events $p = 0.002$, immobility vs. network events $p = 0.002$). The rate of pupil constriction has also been shown to correlate well with cortical population dynamics ([161]). We found that network events primarily occurred during periods of pupil constriction, while no preferential pupil constriction or dilation was observed over the entire immobility period. Locomotor episodes were on average associated with pupil dilation (Fig. 3.3F, repeated measures ANOVA $F_{(2,28)} = 34.18$, $p = 3 \times 10^{-8}$, $n = 6$ mice, data from 3 sessions each, Bonferroni post tests: pupil diameters during locomotion vs. immobility $p = 0.002$, locomotion vs. network events $p = 2.53 \times 10^{-5}$, immobility vs. network events $p = 0.0005$). Together, this suggests that network events are associated with specific pupillary dynamics reflecting substates of arousal and neuronal synchronization during immobility.

The significant cross-correlation between MPP activity with the average GC activity levels during immobility (Fig. 3.1K) suggested the NEs could be driven by MPP input. Thus, we averaged the activity on times of network events and found a significant increase in the level of the MPP signal (Fig. 3.3C, $n = 3$ mice). This analysis shows that at least a subset of NEs coincides with synchronous input from the MPP.

Next, we wondered if self-motion or spatial information is incorporated into NEs and found that both place- and speed cells were similarly recruited into network events (55.42 % of place cells, 42.86 % of speed cells). These results show that MPP-driven network events in immobile animals incorporate neurons that code place- and speed-related information during mobility.

3.3.1 Orthogonality in DG network activity

We further characterized the participation of individual dentate granule cells in network events. We first asked in how far network events involve orthogonal cell populations. Indeed, while individual GCs can partake in multiple network events (Fig. 3.3A, B, network events depicted in different colors), we also observed network events that seemed completely distinct to others. To quantify how similar network events are to one another, we computed population vectors for each individual network event (see section 2.4.1). We then computed the cosine similarity as a measure of similarity between vectors representing individual network events, where identical patterns would have a cosine similarity of 1, and completely orthogonal patterns would exhibit a cosine similarity of 0 (Fig. 3.4A, B). This analysis showed a large fraction of network event pairs that were completely orthogonal to one another, and significantly more than expected by chance (Wilcoxon test, $p < 0.005$ comparison to shuffled data, Fig. 3.4B, C). This is consistent with the capability to represent separate sets of information within network events.

Even though orthogonal network events were observed, we also found a repeated activation of granule cells in multiple network events. To examine if specific sub-ensembles of granule cells are repeatedly recruited in network events, we performed a pairwise Pearson's correlation of the activity of all cell pairs during all network events of a recording session (Fig.

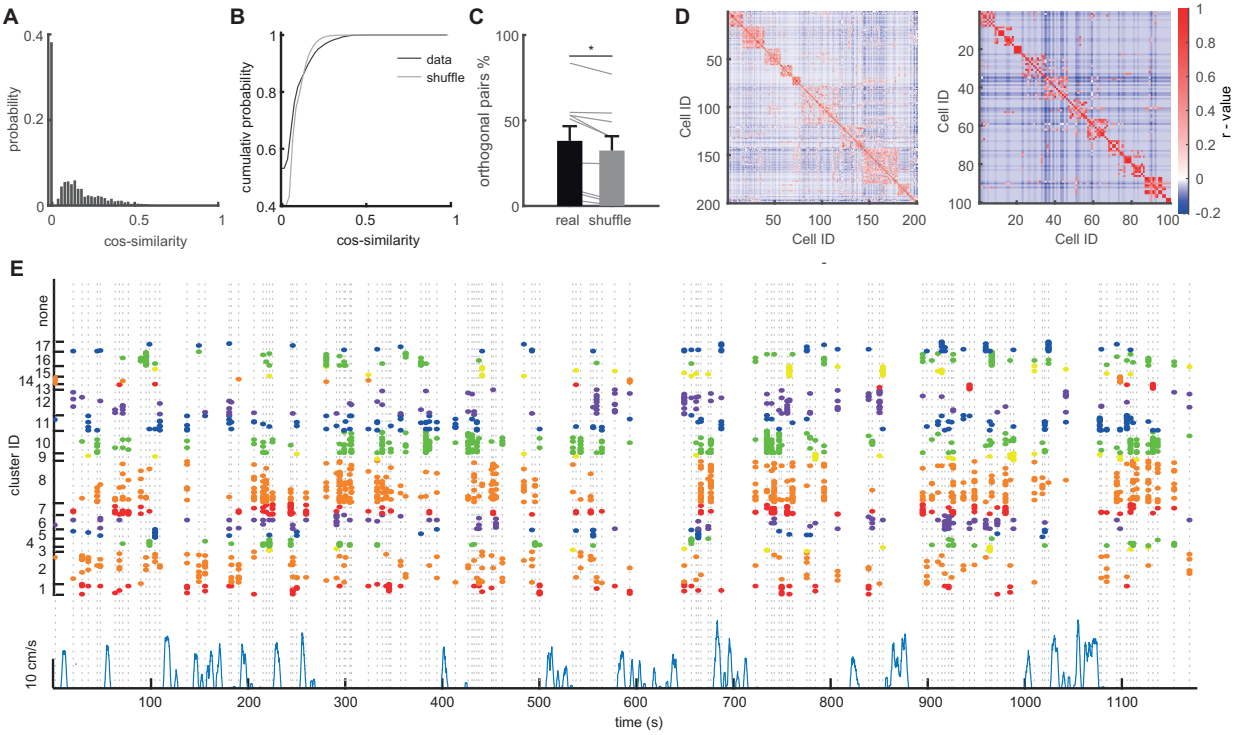

Figure 3.4 – Orthogonality in network events. A, cos-distance between individual NEs. Most events have zero similarity, thus are orthogonal. B, cumulative distribution of cos-similarities (black trace) and from a shuffled distribution (gray traces). Shuffled NEs have a lower fraction of orthogonal pairs as well as highly similar pairs. C, Comparison of orthogonal pairs in real and in shuffled data ($n = 9$). D, Pearson's correlation coefficients off all cell pairs from NE-related activity from two example sessions. High r-values are denoted in red, zero values in white and negative values in blue. Cells are ordered using hierarchical clustering and identified clusters appear as red squares. E, raster plot of cell activity in networks. Cells are ordered according to identified clusters. Running speed is plotted in lower panel (blue trace). Note that NEs related to certain clusters do not appear homogeneously in time.

2.4). Afterwards we reordered the cells using hierarchical clustering (Fig. 3.4D, see section 2.4.4). This analysis shows that subgroups of cells are strongly correlated within network event-related activity. We quantitatively defined clusters as those exhibiting a mean correlation coefficient within the cluster above chance level. Using this definition, we found distinct clusters of correlated cells within network activity with an average cluster size of 6.7 ± 0.4 cells per cluster. The repetitive nature of GC cluster activation during an entire session becomes clearly apparent when viewing cell activity during network events over an entire session, sorted by their participation in clusters (Fig. 3.4G).

3.3.2 The properties of network events in a changed environment

The incorporation of place cells suggests that information about the environment may be represented within network events. We therefore examined if the properties of network events change in the cue-enriched environment.

Dentate gyrus network events were again observed predominantly during immobility (Fig.

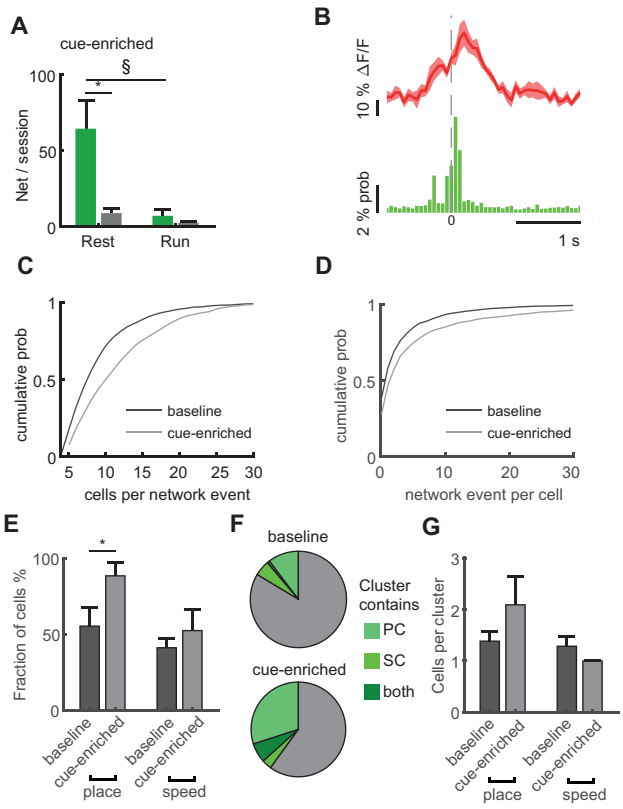

Figure 3.5 – Properties of NE change with the environment. A, The distribution of NE occurrence is unaltered in the cue enriched condition (green bars) and is significant against shuffled data (gray bars) when animals are immobile ($n = 9$). B, MPP bulk activity (red trace) averaged around times of identified NEs (time = 0). GC firing probability (green bars) is highest for network events similarly to baseline condition. C, Network events involve more granule cells in cue-enriched environments. Cumulative probability of network event size (number of cells per network event) for baseline and cue enriched condition (dark and light grey lines, respectively, $n = 9$). D, Cumulative probability of participation in multiple network events per cell for baseline and cue enriched condition (dark and light grey lines, respectively, $n = 9$). E, Fraction of place and speed cells that participate in network events (total number of place/speed cells equals 100 %). F, Relation of place and speed cells to correlated cell clusters. Fraction of the total number of clusters containing place cells (dark green), speed cells (light green), or both (intermediate green). Gray indicates clusters containing neither place nor speed cells. G, Mean number of place and speed cells per cluster, in baseline and cue enriched conditions ($n = 9$ animals).

3.5A) and were similarly coupled to MPP activity (Fig. 3.5B). Increasing the cue density did not significantly alter the network event frequency (2.39 ± 0.73 vs 3.63 ± 0.90 events/minute, respectively, $n = 9$ mice, $F_{(1,30)} = 4.32$, $p = 0.34$). However, the average size of individual network events, measured as the number of participating GCs, was significantly larger in the cue-enriched condition compared to the baseline condition (Fig. 3.5C, Kruskal-Wallis test, $p = 2 \times 10^{-37}$), with individual GCs contributing more frequently to network events in the cue-rich condition (Fig. 3.5D, Kruskal-Wallis test, $p = 2 \times 10^{-26}$). Fewer orthogonal networks were observed in the cue-rich condition, but this was not significantly different to the baseline condition (not shown, Kruskal-Wallis test, n.s. $p = 0.27$).

We then examined if the participation of place and speed cells in network events is altered by increasing sensory cue density. For place cells, the probability of being incorporated in network events was increased significantly (Fig. 3.5E, 55.42 % vs. 88.46 % of place cells in baseline vs. cue-rich conditions), while this was not the case for speed cells (42.86 % vs. 52.63 % of speed cells in baseline vs. cue-rich conditions, χ^2-test regarding changes in the incorporation of place and speed cells in network events $p = 1 \times 10^{-4}$, post-test: place cells baseline vs. cue-enriched $p = 3 \times 10^{-6}$, indicated with asterisk in Fig. 3.5F, speed cells baseline vs. cue-enriched $p = 0.32$). Thus, network events are responsive to changes in the environment and incorporate more place-coding neurons into correlated activity patterns.

The number of correlated cells per cluster within network events did not change in the cue-

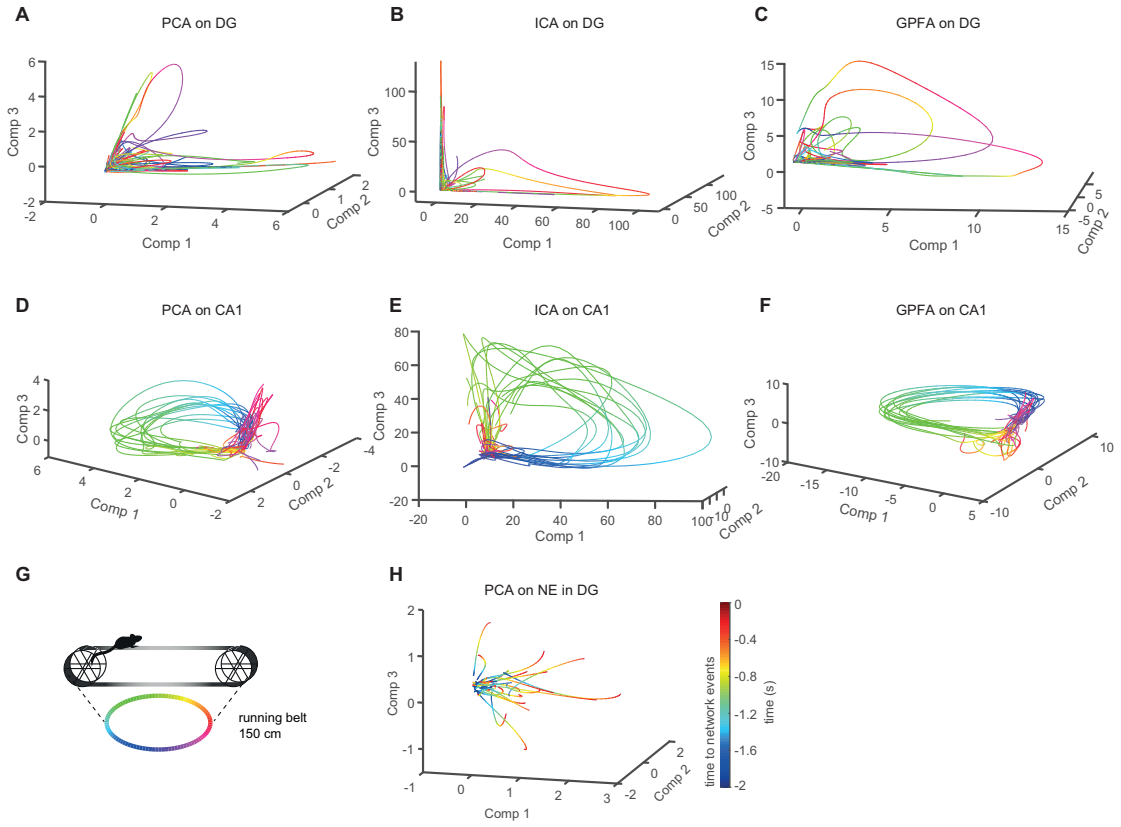

Figure 3.6 – Analysis of population activity in DG and the CA1 subfield of the hippocampus using PCA, ICA and GPFA. A-C, Upper panels depict the first three components from representative sessions (A: PCA, B: ICA, C: GPFA) plotted in a coordinate system. D-F, As in A-C, but for CA1 neurons. Note the smooth and repetitive trajectories. G, Color code for position on the linear track used in panels A-F. H, PCA analysis of population activity associated with network events. Principal components were calculated using data from a 4 s time window (2 s are displayed) around network events during rest. Plotting the first three components resulted in multiple trajectories. The color code refers to the time until occurrence of the network event.

rich condition (cluster size comparison, Kruskal-Wallis test, $p = 0.16$). A significant increase was found in the number of clusters that contained place cells while the number of clusters containing speed cells remained unchanged (Fig. 3.5F, χ^2-test $p = 0.012$, post-test comparison baseline vs. cue-enriched for place cells $p = 0.02$, speed cells $p = 0.20$). While there was only a negligible fraction of clusters that contained both place and speed cells in the baseline condition, this overlap was increased in the cue-enriched condition. Interestingly, the number place or speed cells per cluster was close to one in baseline condition (Fig. 3.5G). There was a trend for slightly higher numbers of PCs per cluster in cue-enriched condition, but generally the number was still close to one. That indicates that there is a one to one mapping of feature cells to correlated clusters.

3.3.3 Similarity of population code during locomotion and network events

The incorporation of place and speed cells in network events, as well as the fact that changing features of the environment modifies network event size and place cell participation is

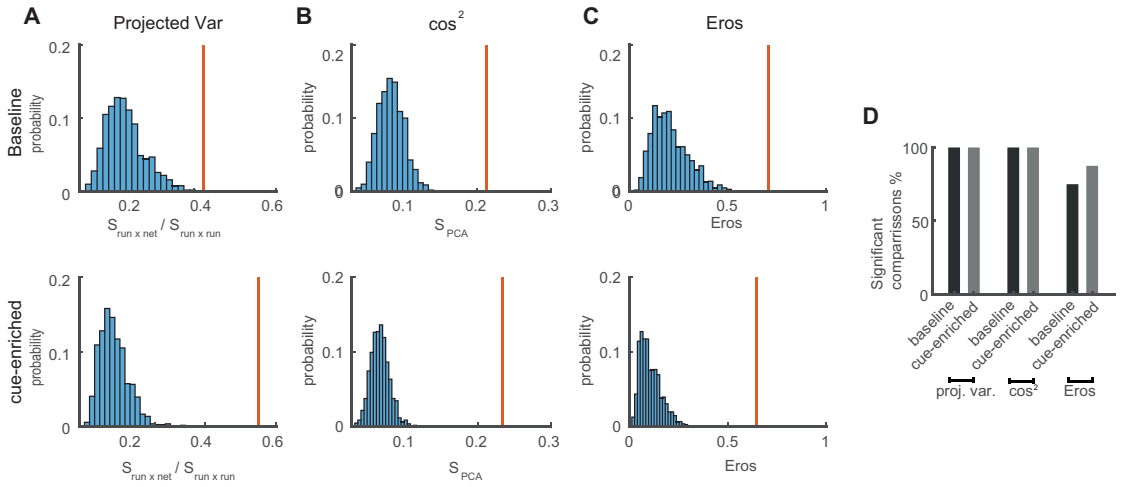

Figure 3.7 – Similarity measures of principle components derived from locomotion related and NE related activity. A, Example for the comparison between real and shuffled data using our developed similarity measure of projected variance. The red line indicates the derived value from data and the blue bars depict the distribution of results from shuffled data. Upper panel: baseline session, lower panel: cue-enriched session. B, Same as in A using the cosine similarity measure. C, Same as in A using the EROS similarity measure. D, Fraction of sessions in which comparisons of population activity were significant vs. chance level for the two cue conditions and all similarity measures ($n = 9$ mice, 1 session per condition).

consistent with the idea that animals, when immobile, represent information about the environment in synchronous, sparse network events. Testing this idea is difficult, however, given that place cells are less prevalent in the dentate gyrus compared to other hippocampal subregions. It has been suggested that the dentate gyrus utilizes a population code [171], meaning that even though only few cells can be rigorously classified as place cells, many more neurons may encode relevant but partial information about the environment. We therefore developed an approach to assess similarity between running and resting activity in the dentate gyrus at the population level (See section 2.4.5). We analyzed population coding during both locomotion and immobility in DG using Principal Component Analysis (PCA) of the activity during individual imaging sessions. We visualized the neuronal state during locomotion captured by the first three components (Fig. 3.6A-C, G, for PCA, Independent Component Analysis, ICA, and Gaussian Process Factor Analysis, GPFA). We observed smooth, large trajectories with high variability reflecting movement along the linear track for some revolutions on the linear treadmill. Because these trajectories did not repeat themselves across multiple rounds, we validated the PCA approaches by applying them to population activity in CA1, in which population codes representing space studied with PCA have been found to be repetitive and stable across different iterations of similar behavior [173]. Indeed, in CA1 trajectories were consistent and stable across multiple rounds and related smoothly to the position on the linear track (Fig. 3.6D-G, for PCA, GPFA, ICA).

To address similarity the between population code during locomotion and during NEs we performed PCA analysis in a split manner (See section 2.4.5). Thus, we performed PCA exclusively of locomotor states and then also performed PCA analysis of the population activity in the same region during network events (Fig. 3.6H). In order to compare the two sets of PCAs representing population activity during running states and network events, respectively, we

first used a vector-based similarity measure. Briefly, we projected the traces recorded during locomotion into the PCA-space representing activity during network events, and tested how much of their variance was captured by them. In this analysis, similarity between both population measures would result in a large fraction of explained variance (Fig. 2.5). To obtain the expected null distribution, we performed a shuffling analysis on the resting activity to eliminate inter-neural correlations (See section 2.4.5). The distributions from shuffled data were clearly distinct from the real data (red vertical line in Fig. 3.7A). In addition to this measure of similarity, we used two further measures based on cosine similarity [168] and EROS [169], testing them against shuffled datasets in the same manner (Fig. 3.7B, C). The comparisons to shuffled data were significant in all sessions, both for baseline and cue-enriched conditions (Fig. 3.7D), indicating that the activity during network events is more similar to activity during locomotion than expected by chance. With these measures, significant comparisons to shuffled data were obtained with all (cosine similarity) or a majority (EROS) of sessions. All three measures thus show that the activity during network events is more similar than expected by chance to sensory-driven activity during locomotion.

Chapter 4

Discussion

The dentate gyrus with its large number of low activity granule cells forms a highly sparse coding network. Its role in sensory driven pattern separation during locomotion in environments has been studied extensively. However, the DG network is also active during immobility and sleep and the role of this activity has been largely unknown.

Studying the DG is challenging, because of GC number, cell layer density and the depth beneath the cortex as well as the CA1 region. In this study, we used large scale dual color two photon imaging to overcome these challenges. The specially designed window (see fig. 2.1C) together with a long working-distance and a high numerical aperture objective allowed visual access to the GC layer to image >300 cells simultaneously. With the chosen mouse model we guaranteed a reliable GCaMP6s labeling of a subset of the GC population, thereby avoiding issues of virally injected GCaMP6s like too high density, unspecific labeling and viruses over expression. The second excitation wavelength enabled us to label the main input structure to DG, the MPP, with the red shifted calcium indicator jRGECO1a (see fig. 2.1A).

This study was designed to investigate input-output computations of the GC population in different behavioral states. While other studies that utilized similar approaches mainly focused on place coding behavior of GCs, we also directed a special focus towards the activity during immobility. By choosing a behavioral design of voluntary locomotion on a blank belt without additional spatial or other cues we minimized external activity trigger that allowed a clean distinction of behavioral state. As expected, the state difference in the MPP-input as well as the DG activity showed prominent characteristics. Further, in both structures we found synchronized activity patterns that were present exclusively during immobility.

In the MPP-input signal of resting animals we observed discrete events of activity in the delta band around 3-4 Hz. In the GC population we found synchronized activity patterns termed network events. We could show several evidences for a correlation between these two activity patterns. DG network events incorporate cells that encode space or speed and are modified with the changes in the environment. These features motivated the theory that NEs not only incorporate spatial information but support the formation of spatial memory. Using population code based similarity measures we could prove the similarity of running-related patterns to NEs.

4.1 State dependent input output computations

4.1.1 Different MPP input patterns during locomotion and immobility

The medial entorhinal cortex contains cells which encode different features of their environment, location and speed [91, 92, 174]. This information is forwarded through the perforant path onto the DG. Even though our imaging technique did not allow differentiation of individual axons in the DG molecular layer measures state depend differences and encoded information from the integrated bulk Ca^{2+}-signal. In line with this, we observed a higher fluorescence amplitude and thus more activity in the MPP axons during locomotion (See Fig. 3.1C). This resulted in a general correlation of speed and MPP bulk-signal (See Fig. 3.1I,J), which could be due to the projection of speed-coding cells as well as the integration of individual grid-cell signals. Indeed, the signal during locomotion followed the speed of the animal consistently and did not show large fluctuations (See fig. 3.1B,3.1H). This was also reflected in a lower variance when comparing the signal during locomotion to states of immobility (See fig. 3.1D). During immobility though the signal showed distinct peaks of activity that occurred at a frequency around 3-4 Hz. This observation is in line with formerly described activity in the δ-band [46] during rest and could be due to reflections of transitions between UP and DOWN states in the MEC [175]. The latter is currently hypothesized to be a part of a general synchronization mechanism between cortex and hippocampus [64]. This mechanism is supposed to be coupled to respiratory behavior of the animal and to support the segregation and integration of information flow between different neuronal networks. Thus, our finding of distinct MPP activity in the δ-band could be a part of this global synchronization mechanism between the MEC and the DG.

4.1.2 State dependent GC activity

GCs are known to show very low activity levels [106, 157, 166], which was also the case in our data. Importantly, for the comparison between studies it is important to take into account how activity is derived and defined from imaging data. The combination of NNMF and activity de-convolution allowed us to identify and include cells into the dataset that showed only one significant event in the whole session. Most cells that showed very sparse activity below < 1 event/min were preferably active during immobility (See Fig. 3.1G). This is important to keep in mind when comparing state differences of individual GCs (See Fig. 3.1E,F) and can explain differences to former imaging studies [166]. Indeed, 60 % of cells in our dataset did not show any running-related activity, thus shifting the mean values of the overall cell populations. On the other hand, for activity levels above 5 events/min we found a higher percentage during locomotion compared to immobility (See Fig. 3.1G inset). Thus, while the mean activity of the whole GC population is lower during locomotion, there is a trend for higher activity cells to be active in that state. This is not exclusive, since some higher active cells are preferably active during immobility in line with a former study that found individual cell activity preferences for both states [157]. Generally it is evident that there is a small fraction of higher active GCs within the population. Higher activity GCs have been previously linked

to larger dendritic trees [103] and newly born GCs [166]. This higher active sub-population may have shaped the idea of GCs as rate coders, since a certain amount of activity is required for a cell to be identified in single unit recordings and correlated to external triggers, like for example place coding [106].

4.1.3 GC place and speed coding

We could identify significant place coding in 2.15% of the GC population using the concept of place preference vectors [166](See Fig. 2.4A, B and Fig. 2.5H). This number was lower compared to other studies [131, 166], which could be due to the big number of low activity neurons as well as our definition of Ca^{2+}-events. When we restrict the analysis to those GCs that showed running related activity, the fraction of significantly place-coding GCs was 23% which matched previously reported values. Additionally, this study was not designed to stimulate strong or stable place coding within the hippocampus since the environment was sparse. The enrichment of running-belts with tactile cues triggered the occurrence of more place cells and could be interpreted as the establishment of a more precise or extensive spatial map (See Fig. 3.2H).

The observed speed correlation in 2.17% of GCs was a surprising result, since it is in contrast to former studies in head fixed mice [157, 166]. On the other hand, speed correlated GCs have been reported in freely moving animals [171, 176] that were also able to decode speed from the GC population. Interestingly, in our data place and speed coders set up two distinct groups within the GC population. The enrichment of the environment did not lead to an increase of SCs (See Fig. 3.2H), in line with the idea the SCs encode a more egocentric parameter that is less modifiable by environmental parameters.

4.2 Synchronized activity during immobility

For very sparse GCs that show singular events of activity it is evident to assume temporal coding rather than rate coding [102]. However, it remained unclear whether synchrony is a necessary feature for the DG network since already single GCs are able to fire efferent CA3 neurons [133]. In this study we found that very sparse events of individual GCs align to synchronized activity patterns that we termed network events (NE, see Fig. 3.3). These events occurred preferably during periods of immobility and the shuffle analysis. Using a shuffle analysis approach we found that NEs during immobility occur significantly more than it could be expected by chance.

Further, we found that NEs mainly appeared when the pupil was contracted or during phases of pupil constriction. Pupil measurements allow the identification of arousal substates within resting periods [161] and an association between pupil constriction and synchronous events has been shown in the visual cortex [172]. Thus the pupil constriction could be a global indicator for synchronization in the brain. Further, the pupil measurements allow an exclusion that the animal was in an aroused state, since arousal would trigger dilution of the pupil.

We could show a correlation of NE occurrence to MPP activity during rest. This finding suggests that at least a subset of NEs is driven by the MPP input. It is very probable that NEs can also be driven by other inputs, mainly the LPP or even recurrent connections from mossy cells or CA3. To answer possible other functional connections further studies are necessary that monitor these input pathways together with GC activity.

4.2.1 Orthogonality of network events

The concept of pattern separation is based on orthogonality of DG representations. This orthogonality within DG was rooted in the sparseness of the DG network [7, 8] Therefore the question was how NEs fit into this concept and whether the activated ensembles were orthogonal to one another. Cosine-distance proved to be a useful tool to measure the orthogonality between the population vectors of NEs and revealed that more than 50 % of NEs were completely orthogonal to each other (See Fig. 3.4A). Further, it showed that NEs were not repeated which the very same composition of cells, since the similarity between NEs never exceeded a value of 0.5. Since the number of participating cells was only ~ 5-7 % of the active GCs, orthogonality could also arise by chance. Though this would still fit the original definition of orthogonality in the DG, we were able to show that the amount of orthogonality in our data is higher than expected from random data (See Fig. 3.4B, C).

Though most NEs were completely orthogonal and the similarity was generally low, there was some overlap between NE population vectors. This overlap was due to higher-active GCs that took part in multiple NEs. We were interested in whether these neurons just randomly participate in NEs, or whether there is a sub-structure within the more active cell population. Using hierarchical clustering, we identified cells that had higher correlation coefficients exclusively within network activity. This analysis showed that the composition of higher active cells is not random, but that sub-ensembles of GCs cluster together (See Fig. 3.4D, E). Additionally, we found that PCs and SCs are distributed into clusters with only one feature cell per cluster both in baseline and cue-enriched sessions. Due to the low number of feature cells in our data it was impossible to prove the one-to-one mapping of clusters, which could be further addressed in future studies with more identified feature cells. Nevertheless, the fact that feature cells did not have high correlation coefficients is further evidence that features are represented orthogonally within the cluster structure.

The orthogonality between NEs together with high correlation coefficients between cells seems to contradict each other. Here it is important to differentiate population code and individual cells. NE population vectors map the population code and our analysis reveals its orthogonality. This finding therefore fits the concept of pattern separation. On the other hand, the high-activity cells within clusters form correlation on an individual basis within the network activity. This repetitiveness might be important to induce Hebbian plasticity in efferent synapses and thus be important for the attractor formation in CA3 [177, 178]. It has been shown in the CA1 region of the hippocampus that comparable types of network activity may trigger plasticity mechanisms in efferent structures and be important for memory consolidation [179]. Further, studies that lesioned DG have shown that the integrity of DG is important for behaviorally relevant firing patterns that determine goal-directed behavior [180].

Thus, the network activity in DG represents features of the environment orthogonally, in line with the concept of pattern separation. At the same time it shows features that might enable it to trigger plasticity in downstream of DG.

4.2.2 DG population code and replay in network events

Repetitive network events are capable of inducing plasticity in the mossy fiber synapses and thus could support the formation of memories. To support memories that are connected to a spatial environment, neuronal representations of aspects of this environment have to be re-activated within network activity [148, 181–183]. We could show that place- as well as speed-cells are activated within network activity (See fig: 3.5E). The relationship between individual network events and certain positions or sequences on the belt could not be investigated in our data. This was due to the low number of feature cells in our data, the fact that feature cells were mostly activated individually in NEs and the circular nature of the belt which makes it impossible to assign whether something happens before or after a certain position on the belt. However, it has been shown that spatial information in the DG population can be decoded even when place cells are actively excluded from that analysis [171]. Thus, spatial information is distributed over the entire ensemble.

DG population code produces orthogonal representations of its input. This is why we used a population measure that splits the information in orthogonal representations, which is principal component analysis (PCA). PCA showed that locomotion epochs produced closed loops in PCA space that did not show a periodicity over rounds (Fig. 3.6A). Thus, we hypothesized that the DG population code maps rounds on the belt as individual epochs. We minimized the probability that this finding was an artifact of the used algorithm by comparing it to other population measures, namely ICA and GPFA, which both produced similar results (Fig. 3.6B, C). The nature of DG population codes becomes more evident in comparison to the hippocampal output population code from the CA1 network. PCA on CA1 imaging data also resulted in closed loops in PCA space, but with a stable representation over rounds (Fig. 3.6D-F). This showed that the running belt was completely and firmly mapped within CA1, while DG produced distinct representations of locomotion epochs.

The concept of replay was first introduced in CA1, where PCs are reactivated in sharp wave ripple network events during immobility [148, 179, 181–183]. These events also recruit orthogonal ensembles but recruit a higher proportion of PCs and active cells [179] compared to the network activity in DG, which made established methods unsuitable for our data. Using PCA to extract key features of population code we analyzed running-related and network-related activity separately to compare the two different PCA spaces and whether they showed a significant amount of similarity. To this end, we developed a novel similarity measure based on projected variances to analyze how much of running related co-variance is mapped in the NE-related PCA space (See section 2.4.5). Using this technique we could show that population codes during locomotion and NEs are indeed more similar than expected by chance (See Fig. 3.7A,D). The comparison to alternative techniques of PCA-basis comparison delivered comparable results in all cases for the cosine similarity method [168] and most cases for EROS [169]. These similarity measures showed that aspects of the population activity

induced by exploration of the relevant environment are recapitulated in DG. Thus, the neuronal activity during resting states is capable to support learning and memory consolidation concerning a particular environment.

4.2.3 Behavioral relevance of network activity

If DG network activity is important for the formation of memories, an impairment of this activity should lead to deficits in dentate dependent learning tasks. It has been shown that even with an impaired DG animals are still able to perform in spatial learning tasks but depend on the DG to distinguish small differences in the environment [10, 12, 127]. A DG dependent spatial learning task is given by a spatial object pattern separation task (OPS task [128]) in which two identical objects are placed in an arena. Between sessions one of the objects is moved to a new position with a defined distance from the original one which triggers a higher motivation for animals to explore the relocated object. The OPS task requires a precise storage of original object positions especially when the displacements between old and new position are small. According to our theory, a disturbance of DG network activity during immobility should be sufficient to downgrade the performance of mice in this task.

In a complementary study the OPS task was established in the lab and its dependence in DG activity was investigated by A. Haubrich [184]. Using the Prox1-Cre mice line, the optogenetic inhibitor halorhodopsin (eNpHR, [185]) was expressed specifically in dentate GCs in both hemispheres (Fig. 4.1A). This silencing approach allowed the determination of the maximal displacement which was indistinguishable for animals when DG was silenced during the entire time the animal spent in the recording chamber (Fig. 4.1B, C). This general conclusion of dentate dependence allowed the investigation to what amount GC silencing would be sufficient to still alter the task performance (Fig. 4.1D). Indeed, it could be shown that optogenetically inhibiting GCs during encoding phase and only when the animals were resting disrupted the capability to distinguish the relocated object (Fig. 4.1E-H, K-N). In comparison, inhibition of GCs during the recall phase did not alter performance (Fig. 4.1I, J, O, P). Thus, these experiments show that activity of GCs during immobility is necessary for the formation of precise memories required for a later pattern separation.

The approach used in the described behavioral experiments impaired all DG activity during immobility and could not be triggered to exclusively inhibit only NEs. Therefore, we cannot exclude the possibility that other kinds of resting activity are required or even sufficient to support memory formation. It has been shown in a closed loop approach that exclusively disrupting DG activity during the occurrence of dentate spikes impairs the performance during trace eyeblink conditioning [186], after this type of behavior has been shown to be dependent on GC activity in general [187]. Therefore, we asked the question whether the found network events are equivalent to at least one kind of dentate spikes.

4.2.4 Are network events dentate spikes?

Synchronized activity in DG has not been described in earlier imaging studies. In studies measuring LFPs in hippocampal regions though, DG network activity has been described,

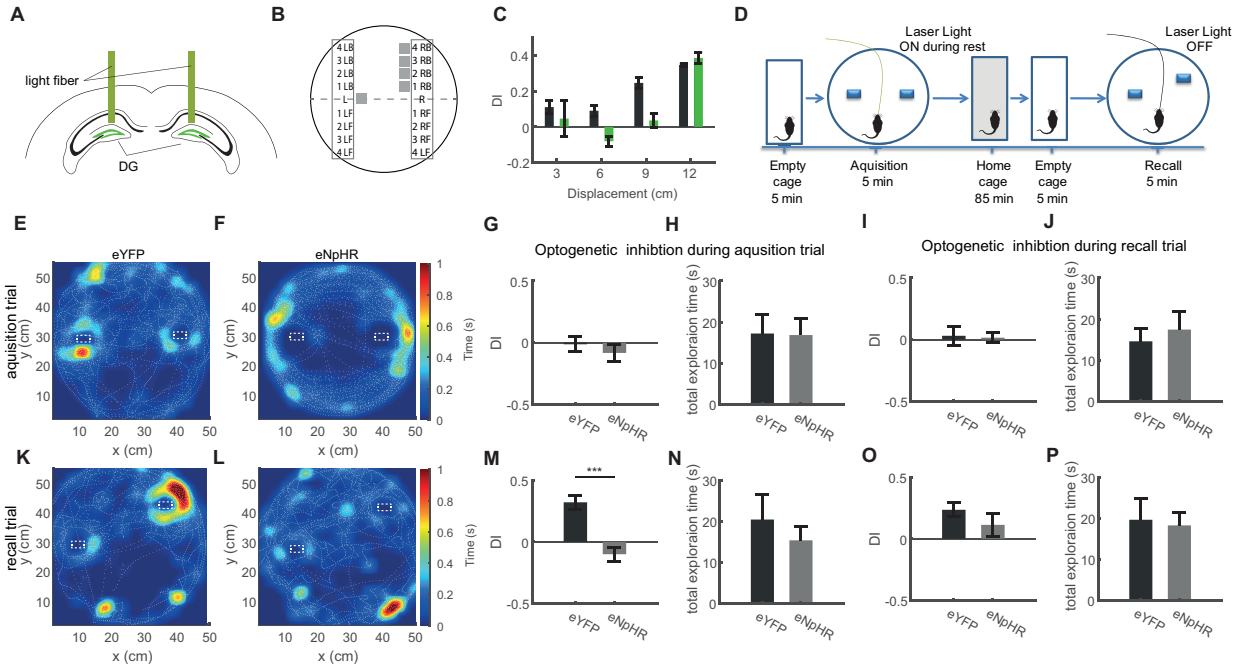

Figure 4.1 – Object pattern separation task during inhibition of dentate granule cell activity during immobility. A, Schematic of the bilateral optogenetic inhibition of the dentate gyrus granule cells expressing eNpHR. B, Schematic of possible object locations for the displaced object. Displacement was randomized for each animal, such that either the left or the right object was displaced, in either a forward or back direction (LB i.e. corresponding to left, backward, and RF to right, forward). The experiment used four possible new locations along a vertical axis, increasing from minor displacement (3 cm) to maximal displacement, indicated by numbers 2-5. C, Results of light-based inhibition of granule cells during acquisition and recall trials for different degrees of object separation indicated on the x-axis (eNpHR group, n=4, green bars) vs. an eYFP expressing control group (n=3, black bars). The effect of granule cell inhibition is most pronounced for intermediate degrees of object movement. D, Schematic of the experimental procedure. In the acquisition phase, mice were familiarized with an arena containing two objects. Following an intermediate period of 90 minutes, the mice were placed in the same arena in which one object was moved slightly. E, F, Representative sessions from acquisition trials in control (eYFP) mice and mice expressing eNpHR in granule cells showing the tracking of the mouse center of mass (dashed white lines), as well as normalized occupancy within the arena. G, Discrimination index from the acquisition trial quantifying the specific exploration activity of the objects relative to one another, with 0 values indicating equal exploration. H, Total time spent exploring the objects in the eYFP and eNpHR groups during the acquisition trial. I, Same as G but with optogenetic inhibition during the recall trial. J, Same as H but with optogenetic inhibition during the recall trial. K, L, Representative sessions from recall trials depicted as shown in B, C. M, Discrimination index for recall trials, showing strong preference for the displaced object in the eYFP group, but not the eNpHR group if granule cell activity was inhibited during acquisition trials only during immobility. N, Total time spent exploring the objects in the eYFP and eNpHR groups during the recall trial (n=6 animals for eNpHR group, n=9 animals for eYFP group). O, Same as M but with optogenetic inhibition during the recall trial. There is a preference for the displaced object in both groups even when cell activity was inhibited during the recall trial. P, Same as N but with optogenetic inhibition during the recall trial. Modified from [184].

namely dentate spikes type 1 and 2 (DS1/2, see section 1.3.2 [101, 155]). In order to prove a connection between LFP and imaging data, it would be necessary to combine these two techniques and correlate these two different read outs. Since this was not the case in our experiments, we can only compare reported features of dentate spikes to the network activity we found in our data.

Like NEs, dentate spikes occur mainly during immobility and, in case of DS2, are driven by MPP input [155]. Further, DSs are reported to be coupled to a synchronization rhythm between cortex and hippocampus in the δ-band [64]. We found that the MPP activity patterns during immobility also fits into this theory and that this input activity partly drives NEs. This coupling of MPP input and NEs fits another report that described wide-spread increases in single-cell activity, gamma oscillations and intraregional gamma coherence during and the DS activity [188].

During DSs it has been shown that GCs depolarize but rarely discharge [101]. In electrode based experiments only a limited number of individual cell activities can be monitored in parallel to LFP measurements and thus the GC population is highly under-sampled. In our data we found that only 5-7 % of active GCs are also active during NEs, where only those cells that are highly active take part in multiple NEs. Therefore, if NE and DS1/2 are identical, the chances of finding a GC that takes part in such an event is very low when only few GCs can be monitored.

Though our experiments can not finally prove that NEs and DSs are identical, we found that both phenomena share similar properties and did not find evidence that these two findings are distinct phenomena.

4.3 Conclusion - Do network events support the formation of memories?

We have described a novel form of sparse, synchronized activity patterns of dentate gyrus granule cells during immobility. We could show that these events fulfill the requirement of orthogonal representations within the DG network. In line with the concept of pattern separation, feature cells are re-activated within this events without temporal overlap. We found repetitive cell-clusters within this activity that may be capable of triggering plasticity mechanisms and instructing the formation of CA3 attractors. The discovered similarity between population codes active during NEs and during locomotion suggests the re-play character of the network activation required for memory consolidation. This is supported by the finding that DG activity during immobility is required for the formation of precise spatial memories. The temporal coupling to afferent structures could suggest the role of NEs in a more distributed organized activity in immobile animals.

In summary, DG network activity may drive synchronous, restricted ensembles in CA3, creating attractor like representations important for the formation of precise memories. Thus it could be part of global synchronization mechanism in immobile animals, required for memory consolidation.

Abbreviations

AP: action potential

BC: basket cell

CA1-3: Cornus Ammonis 1-3

CCK: cholecystokinin

CSF: cerebrospinal fluid

DG: dentate gyrus

DS1/2: dentate spike type 1/2

EC: entorhinal cortex

EPSC: excitatory postsynaptic current

EPSP: excitatory postsynaptic potential

FOV: field of view

GABA: γ-amminobutyric acid

GC: granule cell

GPFA: gaussian process factor analysis

H: hilus

HICAP: hilar commissural-associational path related

ICA: independent component analysis

IPSC: inhibitory postsynaptic current

IPSP: inhibitory postsynaptic potential

LEC: lateral entorhinal cortex

LFP: Local field potential

LPP: lateral perforant path

LTP: long term potentiation

LTD: long term depression

MC: mossy cell

MEC: medial entorhinal cortex

ML: molecular layer

MPP: medial perforant path

MOPP: molecular layer perforant path associated

NA: numerical aperture

NE: network event

OPS task: Object pattern separation task

PC: place cell

PCA: principal component analysis

PV: parvalbumin

SC: speed cell

SL: stratum lucidum

SLM: stratum lacusosum moleculare

SO: stratum oriens

SST: somatostatin

STP: short term potentiation

STD: short term depression

STDP: spike time dependent plasticity

Sub: subiculum

TP: temporoammonic pathway

WD: working distance

Bibliography

1. Kandel, E. R., Schwartz, J. H. & Jessell, T. M. *Principles of Neural Science* (Mc Graw Hill, 2000).
2. Herculano-Houzel, S., Mota, B. & Lent, R. How to build a bigger brain: Cellular scaling rules for rodent brains. *Evolution of Nervous Systems* **3,** 155–166 (2007).
3. Scoville, W. B. & Milner, B. Loss of recent memory after bilateral hippocampal lesions. *Journal of neurology, neurosurgery, and psychiatry* **20,** 11–21 (1957).
4. Lomo, T. Frequency potentiation of excitatory synaptic activity in the dentate area of the hippocampal formation. *Acta Physiologica Scandinavia,* 128 (1966).
5. O'Keefe, J. Place units in the hippocampus of the freely moving rat. *Experimental Neurology* **51,** 78–109 (1976).
6. Cajal, R. y. *Histologie du système nerveux de l'homme & des vertébrés* (Paris, 1909).
7. Marr, D. Simple Memory: A Theory for Archicortex. *Philosophical Transactions of the Royal Society of London. Series B, Biological Sciences* **262,** 23–81 (1971).
8. McNaughton, B. L. & Morris, R. G. Hippocampal synaptic enhancement and information storage within a distributed memory system. *Trends in Neurosciences* **10,** 408–415 (1987).
9. Treves, A. & Rolls, E. T. Computational analysis of the role of the hippocampus in memory. *Hippocampus* **4,** 374–391 (1994).
10. Leutgeb, J. K., Leutgeb, S., Moser, M.-B. & Moser, E. I. Pattern separation in the dentate gyrus and CA3 of the hippocampus. *Science (New York, N.Y.)* **315,** 961–966 (2007).
11. Berron, D. *et al.* Strong evidence for pattern separation in human dentate gyrus. *Journal of Neuroscience* **36,** 7569–7579 (2016).
12. Van Dijk, M. T. & Fenton, A. A. On How the Dentate Gyrus Contributes to Memory Discrimination. *Neuron* **98,** 832–845.e5 (2018).
13. Sakon, J. J. & Suzuki, W. A. A neural signature of pattern separation in the monkey hippocampus. *Proceedings of the National Academy of Sciences of the United States of America* **116,** 9634–9643 (2019).
14. Douglas, R. J. & Martin, K. A. C. A fuctional microcircuit for cat visual cortex. *Journal of Physiology* **440,** 735–769 (1991).

15. Roux, L. & Buzsáki, G. Tasks for inhibitory interneurons in intact brain circuits. *Neuropharmacology* **88,** 10–23 (2015).

16. Buzsáki, G. & Chrobak, J. J. Temporal structure in spatially organized neuronal ensembles: a role for interneuronal networks. *Current Opinion in Neurobiology* **5,** 504–510 (1995).

17. Silver, R. A. Neuronal arithmetic. *Nature Reviews Neuroscience* **11,** 474–489 (2010).

18. Tsumoto, T., Eckart, W. & Creutzfeldt, O. Modification of orientation sensitivity of cat visual cortex neurons by removal of GABA-mediated inhibition. *Exp Brain Research* **34,** 351–63 (1979).

19. Priebe, N. J. & Ferster, D. Direction selectivity of excitation and inhibition in simple cells of the cat primary visual cortex. *Neuron* **45,** 133–145 (2005).

20. Heiss, J. E., Katz, Y., Ganmor, E. & Lampl, I. Shift in the balance between excitation and inhibition during sensory adaptation of S1 neurons. *The Journal of neuroscience : the official journal of the Society for Neuroscience* **28,** 13320–30 (Dec. 2008).

21. Liu, B.-h. *et al.* Structure in Visual Cortex. **13,** 1–21 (2010).

22. Rolls, E. & Treves, A. Neural Networks and Brain Function. *Oxford University Press* (1998).

23. Braganza, O. & Beck, H. The Circuit Motif as a Conceptual Tool for Multilevel Neuroscience. *Trends in Neurosciences* **41,** 128–136 (2018).

24. Goldberg, E. M. & Coulter, D. A. Mechanisms of epileptogenesis: A convergence on neural circuit dysfunction. *Nature Reviews Neuroscience* **14,** 337–349 (2013).

25. Klausberger, T. & Somogyi, P. Neuronal diversity and temporal dynamics: The unity of hippocampal circuit operations. *Science* **321,** 53–57 (2008).

26. Somogyi, P. & Klausberger, T. Defined types of cortical interneurone structure space and spike timing in the hippocampus. *Journal of Physiology* **562,** 9–26 (2005).

27. Carandini, M. & Heeger, D. J. Summation and division by neurons in primate visual cortex. *Science* **264,** 1333–1336 (1994).

28. Miles, R., Toth, K., Gulyas, A. I., Hajos, N. & Tamas, F. F. Differences between Somatic and Dendritic Inhibition in the Hippocampus. *Neuron* **16,** 815–823 (1996).

29. Wilson, N. R., Runyan, C. A., Wang, F. L. & Sur, M. Division and subtraction by distinct cortical inhibitory networks in vivo. *Nature* **488,** 343–348 (2012).

30. Carandini, M. & Heeger, D. J. Normalization as a canonical neural computation. *Nature Reviews Neuroscience* **13,** 51–62 (2012).

31. Olsen, S. R., Bhandawat, V. & Wilson, R. I. Divisive normalization in olfactory population codes. *Neuron* **66,** 287–299 (2010).

32. Pouille, F., Marin-Burgin, A., Adesnik, H., Atallah, B. V. & Scanziani, M. Input normalization by global feedforward inhibition expands cortical dynamic range. *Nature Neuroscience* **12,** 1577–1585 (2009).

33. Royer, S. *et al.* Control of timing, rate and bursts of hippocampal place cells by dendritic and somatic inhibition. *Nature Neuroscience* **15,** 1–10 (2012).

34. Jonke, Z., Legenstein, R., Habenschuss, S. & Maass, W. Feedback inhibition shapes emergent computational properties of cortical microcircuit motifs. *Journal of Neuroscience* **37,** 8511–8523 (2017).

35. De Almeida, L., Idiart, M. & Lisman, J. E. A second function of gamma frequency oscillations: An E%-max winner-take-all mechanism selects which cells fire. *Journal of Neuroscience* **29,** 7497–7503 (2009).

36. Isaacson, J. S. & Scanziani, M. How inhibition shapes cortical activity. *Neuron* **72,** 231–243 (2011).

37. Adesnik, H., Bruns, W., Taniguchi, H., Huang, Z. J. & Scanziani, M. A neural circuit for spatial summation in visual cortex. *Nature* **490,** 226–230 (2012).

38. Hua Liu, B. *et al.* Broad inhibition sharpens orientation selectivity by expanding input dynamic range in mouse simple cells. *Neuron* **71,** 542–554 (2011).

39. Jinde, S., Zsiros, V. & Nakazawa, K. Hilar mossy cell circuitry controlling dentate granule cell excitability. *Frontiers in Neural Circuits* **7,** 1–10 (2013).

40. Hashimotodani, Y. *et al.* LTP at Hilar Mossy Cell-Dentate Granule Cell Synapses Modulates Dentate Gyrus Output by Increasing Excitation/Inhibition Balance. *Neuron* **95,** 928–943.e3 (2017).

41. Lee, W.-C. A. *et al.* Anatomy and function of an excitatory network in the visual cortex. *Nature* **532,** 370–374 (2016).

42. Le Duigou, C., Simonnet, J., Teleñczuk, M. T., Fricker, D. & Miles, R. Recurrent synapses and circuits in the CA3 region of the hippocampus: An associative network. *Frontiers in Cellular Neuroscience* **7,** 1–13 (2014).

43. Letzkus, J. J. *et al.* A disinhibitory microcircuit for associative fear learning in the auditory cortex. *Nature* **480,** 331–335 (2011).

44. Andrew C. Lin, Bygrave, A., De, C. A., Lee, T. & Miesenböck, G. Sparse, Decorrelated Odor Coding in the Mushroom Body Enhances Learned Odor Discrimination. *Nature neuroscience* **17,** 559–568 (2014).

45. Bartos, M., Vida, I., Frotscher, M., Geiger, J. R. & Jonas, P. Rapid signaling at inhibitory synapses in a dentate gyrus interneuron network. *Journal of Neuroscience* **21,** 2687–2698 (2001).

46. Bragin, A. *et al.* Gamma (40-100 Hz) oscillation in the hippocampus of the behaving rat. *Journal of Neuroscience* **15,** 47–60 (1995).

47. Stumpf, C. Drug action on the electrical activity of the hippocampus. *Int. Rev. Neurobiol* **8,** 77–138 (1965).

48. Buzsáki, G., Leung, L. & Vanderwolf, C. Cellular bases of hippocampal EEG in the behaving rat. *Brain Res.* **287,** 139–171 (1983).

49. Csicsvari, J., Jamieson, B., Wise, K. D. & Buzsaki, G. Mechanisms of Gamma Oscillations int he Hippocampus of the Behaving Rat. *Neuron* **37,** 311–322 (2003).

50. Ivan, S. & M., D. Low- and high-frequency membrane potential oscillations during theta activity in CA1 and CA3 pyramidal neurons of the rat hippocampus under ketamine-xylazine anesthesia. *J Neurophysiol.* **70,** 97–116 (1993).

51. Stewart, M. & Fox, S. E. Do septal neurons pace the hippocampal theta rhythm? *Trends in Neurosciences* **13,** 163–169 (1990).

52. Hangya, B., Borhegyi, Z., Szilágyi, N., Freund, T. F. & Varga, V. GABAergic neurons of the medial septum lead the hippocampal network during theta activity. *Journal of Neuroscience* **29,** 8094–8102 (2009).

53. Green, J. D. & Arduini, A. A. Hiipocampal electral activity in arousal. *Journal of Physiology* (1953).

54. Wang, X. J. Pacemaker neurons for the theta rhythm and their synchronization in the septohippocampal reciprocal loop. *Journal of Neurophysiology* **87,** 889–900 (2002).

55. Buzsaki, G. Theta oscillations in the hippocampus. *Neuron* **33,** 325–340 (2002).

56. Vanderwolf, C. H. Hippocampal electrical activity and voluntary movement in the rat. *Electroencephalography and Clinical Neurophysiology* **19,** 165–176 (1968).

57. Whishaw, I. Q. & Vanderwolf, C. H. Hippocampal EEG and behavior: Change in amplitude and frequency of RSA (Theta rhythm) associated with spontaneous and learned movement patterns in rats and cats. *Behavioral Biology* **8,** 461–484 (1973).

58. Sainsbury, R. S., Harris, J. L. & Rowland, G. L. Sensitization and hippocampal type 2 theta in the rat. *Physiology and Behavior* **41,** 489–493 (1987).

59. Buzsáki, G. Neural Syntax: Cell Assemblies, Synapsembles, and Readers. *Neuron* **68,** 362–385 (2010).

60. Buzsaki, G. Theta rhythm of navigation: Link between path integration and landmark navigation, episodic and semantic memory. *Hippocampus* **15,** 827–840 (2005).

61. Ball, G. J., Gloor, P. & Schaul, N. The cortical electromicrophysiology of pathological delta waves in the electroencephalogram of cats. *Electroencephalogr Clin Neurophysiol.* **43,** 346–62 (1977).

62. O'Keefe, J. & Nadel, L. *The Hippocampus as a Cognitive Map* 263–267 (1978).

63. Ito, J. *et al.* Whisker barrel cortex delta oscillations and gamma power in the awake mouse are linked to respiration. *Nature Communications* **5,** 1–10 (2014).

64. Karalis, N. & Sirota, A. Breathing Coordinates Limbic Network Dynamics Underlying Memory Consolidation. *bioRxiv* (2018).

65. Adrian, E. D. & Zotterman, Y. The impulses produced by sensory nerve-endings. *Journal of Physiology* **61,** 49–72 (1926).

66. Hubel, D. H. & Wiesel, T. N. Receptive fields, binocular interaction and functional architecture in the cat's visual cortex. *The Journal of Physiology* **160,** 106–154 (1962).

67. O'Keefe, J., Dostrovsky, J. & J. O'Keefe, J. D. Short Communications The hippocampus as a spatial map . Preliminary evidence from unit activity in the freely-moving rat. *Brain Research* **34,** 171–175 (1971).

68. Quiroga, R. Q., Reddy, L., Kreiman, G., Koch, C. & Fried, I. Invariant visual representation by single neurons in the human brain. *Nature* **435,** 1102–1107 (2005).

69. Barlow, H. B. Single units and sensation: a neuron doctrine for perceptual psychology? *Perception* **1,** 371–94 (1972).

70. Attwell, D. & Laughlin, S. B. An energy budget for signaling in the grey matter of the brain. *Journal of Cerebral Blood Flow and Metabolism* **21,** 1133–1145 (2001).

71. Ince, R. A. A., Senatore, R. & Arabzadeh, E. Information theoretic methods for studying population codes. **23,** 713–727 (2010).

72. Foldiak, P. in *The Handbook of Brain Theory and Neural Networks* (2002).

73. Hebb, D. *The Organization of Behaviour* (Wiley & Sons, 1949).

74. Trappenberg, T. P. *Fundamentals of Computational Neuroscience* (Oxford University Press New York, 2010).

75. Quian Quiroga, R. & Panzeri, S. Extracting information from neuronal populations: Information theory and decoding approaches. *Nature Reviews Neuroscience* **10,** 173–185 (2009).

76. Arabzadeh, E., Panzeri, S. & Diamond, M. E. Deciphering the spike train of a sensory neuron: Counts and temporal patterns in the rat whisker pathway. *Journal of Neuroscience* **26,** 9216–9226 (2006).

77. Oja, E. Simplified neuron model as a principal component analyzer. *Journal of Mathematical Biology* **15,** 267–273 (1982).

78. Bliss, T. V. P. & Lomo, T. long-lasting potentiation of synaptic transmission in the dentate area of the anaesthetized rabbit following stimulation of the perforant path. *Journal of Physiology,* 331–356 (1973).

79. Kelso, S. R., Ganong, A. H. & Brown, T. H. Hebbian synapses in hippocampus. *Proceedings of the National Academy of Sciences of the United States of America* **83,** 5326–5330 (1986).

80. Rolls, E. T. & Kesner, R. P. A computational theory of hippocampal function, and empirical tests of the theory. *Progress in Neurobiology* **79,** 1–48 (2006).

81. Morris, R. in *The Hippocampus Book* 591–617 (2007).

82. Murray, E. A., Baxter, M. G. & Gaffan, D. Monkeys with rhinal cortex damage or neurotoxic hippocampal lesions are impaired on spatial scene learning and object reversals. *Behavioral Neuroscience* **112,** 1291–1303 (1998).

83. Hargreaves, E. L., Rao, G., Lee, I. & Knierim, J. J. Major dissociation between medial and lateral entorhinal input to dorsal hippocampus. *Science (New York, N.Y.)* **308,** 1792–4 (June 2005).

84. Wang, C. *et al.* Egocentric coding of external items in the lateral entorhinal cortex. *Science* **362,** 945–949 (2018).

85. Deshmukh, S. S. & Knierim, J. J. Representation of non-spatial and spatial information in the lateral entorhinal cortex. *Frontiers in Behavioral Neuroscience* **5** (2011).

86. Tsao, A. *et al.* Integrating time from experience in the lateral entorhinal cortex. *Nature* **561,** 57–62 (2018).

87. Hjorth, A. & Jeune, B. Origin and Termination of the Hippocampal Perforant Path in the Rat Studied by Silver Impregnation. *Seven.*

88. Fyhn, M., Molden, S., Witter, M. P., Moser, E. I. & Moser, M. B. Spatial representation in the entorhinal cortex. *Science* **305,** 1258–1264 (2004).

89. Hinman, J. R., Brandon, M. P., Climer, J. R., Chapman, G. W. & Hasselmo, M. E. Multiple Running Speed Signals in Medial Entorhinal Cortex. *Neuron* **91,** 666–679 (2016).

90. Zhang, S.-J. *et al.* Optogenetic Dissection of Entorhinal-Hippocampal Functional Connectivity. *Science* **340,** 35–36 (2013).

91. Brandon, M. P., Koenig, J. & Leutgeb, S. Parallel and convergent processing in grid cell, head-direction cell, boundary cell, and place cell networks. *Wiley Interdisciplinary Reviews: Cognitive Science* **5,** 207–219 (2014).

92. Justus, D. *et al.* Glutamatergic synaptic integration of locomotion speed via septoentorhinal projections. *Nature Neuroscience* **20,** 16–19 (2017).

93. Witter, M. P. Organization of the entorhinal-hippocampal system: A review of current anatomical data. *Hippocampus* **3,** 33–44 (1993).

94. Andersen, P., Morris, R., Amaral, D., Bliss, T. & O'Keefe, J. *The Hippocampus Book* (2009).

95. Steward, O. & Scoville, S. A. Cells of origin of entorhinal cortical afferents to the hippocampus and fascia dentata of the rat. *Journal of Comparative Neurology* **169,** 347–370 (1976).

96. Dannenberg, H. *et al.* Synergy of direct and indirect cholinergic septo-hippocampal pathways coordinates firing in hippocampal networks. *Journal of Neuroscience* **35,** 8394–8410 (2015).

97. Kesner, R. P. & Rolls, E. T. A computational theory of hippocampal function, and tests of the theory: New developments. *Neuroscience and Biobehavioral Reviews* **48,** 92–147 (2015).

98. Bonthius, D. J. *et al.* Use of frozen sections to determine neuronal number in the murine hippocampus and neocortex using the optical disector and optical fractionator. *Brain Research Protocols* **14,** 45–57 (2004).

99. Chawla, M. K. *et al.* Sparse, environmentally selective expression of Arc RNA in the upper blade of the rodent fascia dentata by brief spatial experience. *Hippocampus* **15,** 579–586 (2005).

100. Jung, M. W. & McNaughton, B. L. Spatial selectivity of unit activity in the hippocampal granular layer. *Hippocampus* **3,** 165–182 (1993).

101. Penttonen, M., Kamondi, A., Sik, A., Acsády, L. & Buzsáki, G. Feed-forward and feedback activation of the dentate gyrus in vivo during dentate spikes and sharp wave bursts. *Hippocampus* **7,** 437–450 (1997).

102. Pernía-Andrade, A. & Jonas, P. Theta-Gamma-Modulated Synaptic Currents in Hippocampal Granule Cells InVivo Define a Mechanism for Network Oscillations. *Neuron* **81,** 140–152 (2014).

103. Diamantaki, M., Frey, M., Berens, P., Preston-Ferrer, P. & Burgalossi, A. Sparse activity of identified dentate granule cells during spatial exploration. *eLife* **5,** 1–17 (2016).

104. Spruston, N. & Johnston, D. Perforated patch-clamp analysis of the passive membrane properties of three classes of hippocampal neurons. *Journal of Neurophysiology* **67,** 508–529 (1992).

105. Staley, K. J., Otis, T. S. & Mody, I. Membrane properties of dentate gyrus granule cells: Comparison of sharp microelectrode and whole-cell recordings. *Journal of Neurophysiology* **67,** 1346–1358 (1992).

106. Leutgeb, J. K. & Moser, E. I. Enigmas of the Dentate Gyrus. *Neuron* **55,** 176–178 (2007).

107. Krueppel, R., Remy, S. & Beck, H. Dendritic integration in hippocampal dentate granule cells. *Neuron* **71,** 512–528 (2011).

108. Rolls, E. T. A Unifying Computational Neuroscience Approach. *Oxford University Press* (2008).

109. Rolls, E. T. Functions of neuronal networks in the hippocampus and cerebral cortex in memory. *Cambridge University Press,* 15–33 (1989).

110. Hasselmo, M. E. & Wyble, B. P. Free recall and recognition in a network model of the hippocampus: simulating effects of scopolamine on human memory function. *Behavioural Brain Research* **89,** 1–34 (1997).

111. Ewell, L. A. & Jones, M. V. Frequency tuned distribution of inhibition in the dentate gyrus. *The Journal of neuroscience : the official journal of the Society for Neuroscience* **30,** 12597–12607 (2010).

112. Espinoza, C., Guzman, S. J., Zhang, X. & Jonas, P. Parvalbumin interneurons obey unique connectivity rules and establish a powerful lateral-inhibition microcircuit in dentate gyrus. *Nature Communications* **9,** 1–10 (2018).

113. Braganza, O., Müller-Komorowska, D., Kelly, T. & Beck, H. Quantitative properties of a feedback circuit predict frequency-dependent pattern separation. *eLife* (2019).

114. Halasy, K. & Somogyi, P. Subdivisions in the Multiple GABAergic Innervation of Granule Cells in the Dentate Gyrus of the Rat Hippocampus. *European Journal of Neuroscience* **5,** 411–429 (1993).

115. Freund, T. F. & Buzsaki, G. Interneurons of the Hippocampus. *Hippocampus* **6,** 347–470 (1996).

116. Hu, H., Gan, J. & Jonas, P. Fast-spiking, parvalbumin positiv GABAergic interneurons: From cellular design to microcircuit function. *Science* **345** (2014).

117. Zipp, F., Nitsch, R., Soriano, E. & Frotscher, M. Entorhinal fibers form synaptic contacts on parvalbumin-immunoreactive neurons in the rat fascia dentata. *Brain Research* **495,** 161–166 (1989).

118. Geiger, J. R., Lübke, J., Roth, a., Frotscher, M. & Jonas, P. Submillisecond AMPA receptor-mediated signaling at a principal neuron-interneuron synapse. *Neuron* **18,** 1009–23 (June 1997).

119. Han, Z. S., Buhl, E. H., Loerinczi, Z. & Somogyi, P. A High Degree of Spatial Selectivity in the Axonal and Dendritic Domains of Physiologically Identified Local circuit Neurons in the Dentate Gyms of the Rat Hippocampus. *European Journal of Neuroscience* **5,** 395–410 (1993).

120. Scharfman, H. E. & Myers, C. E. Hilar mossy cells of the dentate gyrus: A historical perspective. *Frontiers in Neural Circuits* **6,** 1–17 (2012).

121. Nakazawa, K. Dentate Mossy Cell and Pattern Separation. *Neuron* **93,** 465–467 (2017).

122. Bui, A. D. *et al.* Dentate gyrus mossy cells control spontaneous convulsive seizures and spatial memory. *Science* **790,** 787–790 (2018).

123. Treves, A., Tashiro, A., Witter, M. E. & Moser, E. I. What is the mammalian dentate gyrus good for? *Neuroscience* **154,** 1155–1172 (2008).

124. Rolls, E. T. The mechanisms for pattern completion and pattern separation in the hippocampus. *Frontiers in Systems Neuroscience* **7,** 1–21 (2013).

125. Jazayeri, M. & Afraz, A. Navigating the Neural Space in Search of the Neural Code. *Neuron* **93,** 1003–1014 (2017).

126. Cayco-Gajic, N. A. & Silver, R. A. Re-evaluating Circuit Mechanisms Underlying Pattern Separation. *Neuron* **101,** 584–602 (2019).

127. McHugh, T. J. *et al.* Dentate Gyrus NMDA Receptors Mediate Rapid Pattern Separation in the Hippocampal Network. *Science* **317,** 1826–1830 (2007).

128. Van Goethem, N. P., van Hagen, B. T. & Prickaerts, J. Assessing spatial pattern separation in rodents using the object pattern separation task. *Nature Protocols* **13,** 1763–1792 (2018).

129. Neunuebel, J. P. & Knierim, J. J. CA3 retrieves coherent representations from degraded input: Direct evidence for CA3 pattern completion and dentate gyrus pattern separation. *Neuron* **81,** 416–427 (2014).

130. Allegra, M., Posani, L. & Schmidt-hieber, C. The hippocampus as a perceptual map : neuronal and behavioral discrimination during memory encoding (2019).

131. Hainmueller, T. & Bartos, M. Parallel emergence of stable and dynamic memory engrams in the hippocampus. *Nature* **558,** 292–296 (2018).

132. Amaral, D. G. & Witter, M. P. The three-dimensional organization of the hippocampal formation: A Review of anatomical data. *Neuroscience* **31,** 571–591 (1989).

133. Henze, D. A., Wittner, L. & Buzsáki, G. Single granule cells reliably discharge targets in the hippocampal CA3 network in vivo. *Nature Neuroscience* **5,** 790–795 (2002).

134. Bonifazi, P. *et al.* GABAergic hub neurons orchestrate synchrony in developing hippocampal networks. *Science (New York, N.Y.)* **326,** 1419–24 (Dec. 2009).

135. Hopfield, J. J. Neural networks and physical systems with emergent collective computational abilities. *Proc. Natl. Acad. Sci. U. S. A.* **79,** 2554–2558 (1982).

136. Rolls, E. T. An attractor network in the hippocampus: Theory and neurophysiology. *Learning and Memory* **14,** 714–731 (2007).

137. Barak, O., Rigotti, M. & Fusi, S. The sparseness of mixed selectivity neurons controls the generalization-discrimination trade-off. *Journal of Neuroscience* **33,** 3844–3856 (2013).

138. Myers, C. E. & Scharfman, H. E. A Role for hilar cells in pattern separation in the dentate gyrus: A computational approach. *Hippocampus* **19,** 321–337 (2009).

139. Li, X. G., Somogyi, P., Ylinen, A. & Buzsáki, G. The hippocampal CA3 network: An in vivo intracellular labeling study. *Journal of Comparative Neurology* **339,** 181–208 (1994).

140. Pothmann, L. *et al.* Function of inhibitory micronetworks is spared by Na+ channel-acting anticonvulsant drugs. *Journal of Neuroscience* **34,** 9720–9735 (2014).

141. Megias, M., Emri, Z., Freund, T. F. & Gulyás, A. I. Total number and distribution of inhibitory and excitatory synapses on hippocampal CA1 pyramidal cells. *Neuroscience* **102,** 527–540 (2001).

142. Lehn, H. *et al.* A specific role of the human hippocampus in recall of temporal sequences. *Journal of Neuroscience* **29,** 3475–3484 (2009).

143. Vago, D. R. & Kesner, R. P. Disruption of the direct perforant path input to the CA1 subregion of the dorsal hippocampus interferes with spatial working memory and novelty detection. *Behavioral Brain Research* **189,** 273–283 (2008).

144. Muller, R. U. & Kubie, J. L. The effects of changes in the environment on the spatial firing of hippocampal complex-spike cells. *Journal of Neuroscience* **7,** 1951–1968 (1987).

145. Fuhrmann, F. *et al.* Locomotion, Theta Oscillations, and the Speed-Correlated Firing of Hippocampal Neurons Are Controlled by a Medial Septal Glutamatergic Circuit. *Neuron* **86,** 1253–1264 (2015).

146. O'Keefe, J. & Recce, M. L. Phase Relationship Between Hippocampal Place Units and the EEG Theta Rhythm. *Hyppocampus* **3,** 317–330 (1993).

147. Dragoi, G. & Buzsáki, G. Temporal Encoding of Place Sequences by Hippocampal Cell Assemblies. *Neuron* **50,** 145–157 (2006).

148. Skaggs, W. E., McNaughton, B. L., Wilson, M. A. & Barnes, C. A. Theta phase precession in hippocampal neuronal populations and the compression of temporal sequences. *Hippocampus* **6,** 149–172 (1996).

149. Bender, F. *et al.* Theta oscillations regulate the speed of locomotion via a hippocampus to lateral septum pathway. *Nature Communications* **6** (2015).

150. Csicsvari, J., Hirase, H., Czurkó, A., Mamiya, A. & Buzsáki, G. Oscillatory coupling of hippocampal pyramidal cells and interneurons in the behaving rat. *Journal of Neuroscience* **19,** 274–287 (1999).

151. Ekstrom, A. D., Meltzer, J., McNaughton, B. L. & Barnes, C. A. NMDA Receptor Antagonism Blocks Experience-Dependent Expansion of Hippocampal "Place Fields". *Neuron* **31,** 1–8 (2001).

152. McNaughton, B. L., Barnes, C. A. & O'Keefe, J. The contributions of position, direction, and velocity to single unit activity in the hippocampus of freely-moving rats. *Experimental Brain Research* **52,** 41–49 (1983).

153. Freund, T. F., Katona, I. & Piomelli, D. Role of endogenous cannabinoids in synaptic signaling. *Physiological Reviews* **83,** 1017–1066 (2003).

154. De Almeida, L., Idiart, M. & Lisman, J. E. Memory retrieval time and memory capacity of the CA3 network: Role of gamma frequency oscillations. *Learning and Memory* **14,** 795–806 (2007).

155. Bragin, A., Jando, G., Nadasdy, Z., Van Landeghem, M. & Buzsaki, G. Dentate EEG spikes and associated interneuronal population bursts in the hippocampal hilar region of the rat. *Journal of Neurophysiology* **73,** 1691–1705 (1995).

156. Penttonen, M., Kamondi, A., Acsády, L. & Buzsáki, G. Gamma frequency oscillation in the hippocampus of the rat: Intracellular analysis in vivo. *European Journal of Neuroscience* **10,** 718–728 (1998).

157. Pilz, G. A. *et al.* Functional imaging of dentate granule cells in the adult mouse hippocampus. *Journal of Neuroscience* **36,** 7407–7414 (2016).

158. Dana, H. *et al.* Thy1-GCaMP6 transgenic mice for neuronal population imaging in vivo. *PLoS ONE* **9** (2014).

159. Dana, H. *et al.* Sensitive red protein calcium indicators for imaging neural activity. *eLife* **5,** 1–24 (2016).

160. Bernal Sierra, Y. A. *et al.* Potassium channel-based optogenetic silencing. *Nature Communications* **9,** 1–13 (2018).

161. Reimer, J. *et al.* Pupil Fluctuations Track Fast Switching of Cortical States during Quiet Wakefulness. *Neuron* **84,** 355–362 (2014).

162. Dombeck, D. A., Khabbaz, A. N., Collman, F., Adelman, T. L. & Tank, D. W. Imaging Large-Scale Neural Activity with Cellular Resolution in Awake, Mobile Mice. *Neuron* **56,** 43–57 (2007).

163. Yizhar, O., Fenno, L. E., Davidson, T. J., Mogri, M. & Deisseroth, K. Optogenetics in neural systems. *Neuron* **71,** 9–34 (2011).

164. Greenberg, D. S. & Kerr, J. N. Automated correction of fast motion artifacts for two-photon imaging of awake animals. *Journal of Neuroscience Methods* **176,** 1–15 (2009).

165. Pnevmatikakis, E. A. *et al.* Simultaneous Denoising, Deconvolution, and Demixing of Calcium Imaging Data. *Neuron* **89,** 285 (2016).

166. Danielson, N. B. *et al.* Distinct Contribution of Adult-Born Hippocampal Granule Cells to Context Encoding. *Neuron* **90,** 101–112 (2016).

167. Cunningham, J. P. & Yu, B. M. Dimensionality reduction for large-scale neural recordings. *Nature Neuroscience* **17,** 1500–1509 (2014).

168. Krzanowski, W. J. Between-Groups Comparison of Principal Components. *Journal of the American Statistical Association* **74,** 386–703–707 (1979).

169. Yang, K. & Shahabi, C. A PCA-based Similarity Measure for Multivariate Time Categories and Subject Descriptors. *Mmdb'04,* 65–74 (2004).

170. Neunuebel, J. P. & Knierim, J. J. Spatial firing correlates of physiologically distinct cell types of the rat dentate gyrus. *Journal of Neuroscience* **32,** 3848–3858 (2012).

171. Stefanini, F. *et al.* A distributed neural code in the dentate gyrus and CA1. *bioRxiv,* 292953 (2019).

172. Reimer, J. *et al.* Pupil fluctuations track rapid changes in adrenergic and cholinergic activity in cortex. *Nature Communications* **7,** 1–7 (2016).

173. Rubin, A. *et al.* Revealing neural correlates of behavior without behavioral measurements. *Nature Communications* **10** (2019).

174. Hafting, T., Fyhn, M., Molden, S., Moser, M. B. & Moser, E. I. Microstructure of a spatial map in the entorhinal cortex. *Nature* **436,** 801–806 (2005).

175. Sirota, A. & Buzsaki, G. Interaction between neocortical and hippocampal networks via slow oscillations. *Thalamus and Related Systems* **3,** 245–259 (2005).

176. Murano, T. *et al.* Multiple types of navigational information is diffusely and independently encoded in the population activities of the dentate gyrus neurons. *bioRxiv,* 2020 .06.09.141572 (2020).

177. O'Reilly, R. C. & McClelland, J. L. Hippocampal conjunctive encoding, storage, and recall: Avoiding a trade off. *Hippocampus* **4,** 661–682 (1994).

178. GoodSmith, D. *et al.* Spatial Representations of Granule Cells and Mossy Cells of the Dentate Gyrus. *Neuron* **93,** 677–690.e5 (2017).

179. Malvache, A., Reichinnek, S., Villette, V. & Haimerl, C. Awake hippocampal reactivations project onto orthogonal neuronal assemblies. *Science* **353** (2016).

180. Sasaki, T. *et al.* Dentate network activity is necessary for spatial working memory by supporting CA3 sharp-wave ripple generation and prospective firing of CA3 neurons. *Nature Neuroscience* **21,** 258–269 (2018).

181. Wilson, M. A. & McNaughton, B. L. Reactivation of Hippocampal Ensemble Memories During Sleep. *Science* **265,** 14–17 (1994).

182. Foster, D. J. & Wilson, M. A. Reverse replay of behavioural sequences in hippocampal place cells during the awake state. *Nature* **440,** 680–683 (2006).

183. Diba, K. & Buzsáki, G. Forward and reverse hippocampal place-cell sequences during ripples. *Nature Neuroscience* **10,** 1241–1242 (2007).

184. Pofahl, M. *et al.* Dentate gyrus population activity during immobility supports formation of precise memories. *bioRxiv,* 2020.03.05.978320 (2020).

185. Gradinaru, V. *et al.* Targeting and readout strategies for fast optical neural control in vitro and in vivo. *Journal of Neuroscience* **27,** 14231–14238 (2007).

186. Nokia, M. S., Gureviciene, I., Waselius, T., Tanila, H. & Penttonen, M. Hippocampal electrical stimulation disrupts associative learning when targeted at dentate spikes. *Journal of Physiology* **595,** 4961–4971 (2017).

187. Madronal, N. *et al.* Rapid erasure of hippocampal memory following inhibition of dentate gyrus granule cells. *Nature Communications* **7,** 1–10 (2016).

188. Headley, D. B., Kanta, V. & Paré, D. Intra-and interregional cortical interactions related to sharp-wave ripples and dentate spikes. *Journal of Neurophysiology* **117,** 556–565 (2017).

Acknowledgments

It has been a long journey and I had the honor of getting to know a lot of great people along the way, some of which I want to say thank you. First of all, I want to thank Prof. Dr. Heinz Beck who gave me the opportunity to experience the enormous fun of conducting a Ph.D. thesis in his lab. I am very grateful for the trust he put in the project and me, even in times when I did not trust myself nor knew what I was doing. I very much enjoyed to share passions with him that reached from Bach, coffee, lasers and sometimes even neuroscience. To work "together with" rather than "for" your supervisor is not self-evident, and I am happy and proud to call Heinz my friend (officially after my defense, I suppose). Thanks to Prof. Dr. Walter Witke who agreed on co-supervising this thesis and who represents the Faculty of Math and Natural Sciences. I am very thankful to Dr. Laura Ewell who joint the crazy ride that this project sometimes was and who very much helped to keep it on track. Her true love for science, the humble use of her impressive knowledge, and all of this while always being friendly and respectful to everyone around her are truly inspiring qualities and made it a joy to work with her. I want to thank Prof. Dr. Jakob Macke for his mathematical advices and help.

I want to thank Negar Nikbakht. Together we started our projects in a big empty room and during all the years that came afterwards we shared all the ups and downs that somehow brought us to a good end. I guess the fact that we still get along with each other is a good indicator of our friendship. Thanks to Theresa Nguyen, Andre Haubrich, Dr. Oliver Braganza and Dr. Kurtulus Gölcük for their contribution to my project by designing, establishing and conducting the OPS task all based on some funny hypothesis we had. Thanks to Pedro Royero, Nicola Masala, Daniel Müller, Fabian Distler and Dr. Leonie Pothmann for all the good times in the lab, the office, the coffee corner, at Alter Zoll and on all the conferences. I am very thankful to Dr. Tony Kelly and Dr. Thoralf Opitz whose experience, advice and friendship meant a lot to me. Special thanks to Milan Pabst, who is unfortunately not with us anymore. Besides many useful things I learned from him it was he who taught me that only a good espresso is a good espresso. Another person involved in this project who passed away too early and whom I want to thank, is Klaus Granitza. In his workshop he brought life to all of our designs and without him this project would have been impossible. Thanks to my Mother and Father who always backed me up in every situation. You are the solid rock I built my life upon. Thank you Susi, for you are home.

Statement

I hereby certify that the work presented here was accomplished by myself and without the use of illegitimate means or support, and that no sources ant tools were used other than those cited.

Bonn, August 18, 2020